

# 1 A potential link between waterfall recession rate and 2 bedrock channel concavity

Eitan Shelef,<sup>1,2</sup> Itai Haviv,<sup>2</sup> Liran Goren,<sup>2</sup>

---

Corresponding author: Eitan Shelef, Department of Geological & Environmental Science, University of Pittsburgh, Pittsburgh, PA, 15260. (shelef@pitt.edu)

<sup>1</sup>Department of Geological & Environmental Science, University of Pittsburgh, Pittsburgh, PA, USA.

<sup>2</sup>Department of Geological and Environmental Sciences, Ben Gurion University, Beer Sheva, Israel.

**Abstract.**

4 The incision of bedrock channels is typically modeled through the stream  
5 power or the shear stress applied on the channel bed. However, this ap-  
6 proach is not valid for quasi-vertical knickpoints (hereafter waterfalls),  
7 where water and sediments do not apply direct force on the vertical face  
8 and waterfall retreat rate is often modeled as a power function of drainage  
9 area. These different incision modes are associated with two measurable  
10 exponents: the channel concavity,  $\theta$ , that is measured from the channel to-  
11 pography and is used to evaluate the exponents of drainage area and slope  
12 in the channel incision model, and  $p$ , that is measured from the location  
13 of waterfalls within watersheds, and evaluates the dependency of the wa-  
14 terfall recession rate on drainage area. To better understand the relations  
15 between channel incision and waterfall recession we systematically compare  
16 between the exponents  $p$  and  $\theta$ . These parameters were computed from dig-  
17 ital elevation models (30 m SRTM) of 12 river basins with easily detectable  
18 waterfalls. We show that  $p$  and  $\theta$  are: (1) similar within uncertainty, (2)  
19 come from a similar distribution, and (3) covary for networks with a large  
20 number of waterfalls ( $\gtrsim 10$ ). In the context of bedrock incision models this  
21 hints that the same processes govern waterfall retreat rate and the inci-  
22 sion of non-vertical channel reaches in the analyzed basins, and/or that  
23 downstream incision can dictate waterfall retreat rate.

## 1. Introduction

Quantification of landscape response to climatic and tectonic changes is a key component in predicting topographic sensitivity to future changes, and in reconstructing past changes from topographic patterns [e.g., *Whipple and Tucker, 1999; Crosby and Whipple, 2006; Moon et al., 2011; Goren, 2016*]. In bedrock landscapes, the rate of channel incision ( $E$  [L/T]) is governed by complex interactions between discharge and channel geometry, as well as sediment and bedrock properties [e.g., *Seidl and Dietrich, 1992; Dietrich et al., 2003; Gasparini et al., 2006*]. This rate is often described as a function of gravitationally induced shear-stress or stream-power applied to the channel bed [e.g., *Bagnold, 1966; Howard and Kerby, 1983; Whipple and Tucker, 1999; Tucker and Hancock, 2010*], and formulated as:

$$E = K A^m S^n, \tag{1}$$

where  $K$  [ $L^{1-2m}/T$ ] is termed the erodibility coefficient and depends on bedrock properties, discharge-drainage area relations, and channel geometry.

In this framework, an increased rate of base-level fall ( $U$  [L/T]) is communicated to the upper reaches of the channel network through upstream recession of oversteepened channel segments, namely, knickpoints [e.g., *Rosenbloom and Anderson, 1994; Whipple and Tucker, 1999; Bishop et al., 2005; Crosby and Whipple, 2006*]. When the knickpoint is non-vertical, its recession rate (i.e., knickpoint celerity:  $C_e$  [L/T]) can be derived from the channel incision model (equation (1)) [*Rosenbloom and Anderson, 1994; Whipple and Tucker, 1999; Bishop et al., 2005; Haviv et al., 2006; Berlin and Anderson, 2007*]:

$$C_e = K A^m S^{n-1}. \tag{2}$$

43 The celerity,  $C_e$ , is independent of the slope ( $S$ ) in two commonly assumed scenarios:  
 44 (1) when  $n = 1$  [*Rosenbloom and Anderson, 1994; Berlin and Anderson, 2007*], such  
 45 that  $m/n = m$ , and (2) when the slope of the knickpoint is the slope predicted for a  
 46 steady state landscape under the new rate ( $U_n$ ) of base level fall (i.e.,  $U_n = E$  such that  
 47  $S = (\frac{U_n}{K})^{1/n} A^{-m/n}$  can be substituted into equation (2)). In both cases equation (2)  
 48 results in

$$C_e \propto A^{m/n}, \quad (3)$$

49 where in the latter case  $C_e$  also depends on  $U$  [e.g., *Niemann et al., 2001; Wobus et al.,*  
 50 *2006b*].

51 When  $U$  and  $K$  are generally uniform along the channel, the ratio  $m/n$  equals the  
 52 channel concavity index,  $\theta$ , that is typically computed from linear relations between  $\log(S)$   
 53 and  $\log(A)$  or between topographic elevation. In that case, equation (3) becomes:

$$C_e \propto A^\theta. \quad (4)$$

54 When a knickpoint is quasi vertical (i.e., a waterfall) such that water and sediment  
 55 fall without applying direct force on the knickpoint face, the assumptions that underly  
 56 Equations 1 and 2 become invalid [*Crosby and Whipple, 2006; Haviv et al., 2010*]. In  
 57 that case, waterfall recession is influenced by a variety of processes, including plunge-  
 58 pool drilling, freeze-thaw and wet-dry cycles, and groundwater seepage. The intensity of  
 59 these processes depends on factors such as cap-rock and sub-cap-rock strength and joint  
 60 density, sediment concentration and grain-size distribution, water discharge, the micro-  
 61 topography of the waterfall lip, the waterfall height, temperature and rainfall fluctuations,  
 62 water jet impact angle, and the properties of the lag-debris [e.g., *Gilbert, 1907; Mason and*

63 *Arumugam*, 1985; *Howard and Kochel*, 1988; *Haviv et al.*, 2006; *Lamb et al.*, 2007; *Haviv*  
 64 *et al.*, 2010; *Lamb et al.*, 2014; *Mackey et al.*, 2014; *Scheingross et al.*, 2017]. Whereas  
 65 this suggests that multiple factors should be parameterized to accurately model waterfall  
 66 celerity [e.g., *Lamb et al.*, 2006; *Haviv et al.*, 2010; *Scheingross and Lamb*, 2016], a simple  
 67 model for waterfall celerity ( $C_{ew}$  [L/T]) was posited by *Crosby and Whipple* [2006] and  
 68 explored in various settings [*Crosby and Whipple*, 2006; *Berlin and Anderson*, 2007; *Haviv*,  
 69 2007; *DiBiase et al.*, 2015; *Mackey et al.*, 2014; *Brocard et al.*, 2016]:

$$C_{ew} = BA^p, \quad (5)$$

70 where  $B$  [ $L^{1-2p}/T$ ] is a proportionality constant, and  $p$  is a positive exponent. In this  
 71 model both  $B$  and  $p$  are not necessarily related to an incision model such as the one  
 72 presented in equation (1).

73 The different geometry of waterfalls and non-vertical knickpoints suggests that their re-  
 74 cession rate might be governed by different processes, where the recession of non-vertical  
 75 knickpoints is often formulated based on the bedrock channel incision model (equation  
 76 (2)), and that of waterfalls (i.e., equation (5)) is based on empirically demonstrated re-  
 77 lations with drainage area [e.g., *Berlin and Anderson*, 2007; *Crosby and Whipple*, 2006].  
 78 However, the similarity in the functional form of equations 4 and 5 suggests a potential  
 79 link between the two rates, and highlights the need for a systematic comparison between  $\theta$   
 80 and  $p$ . Such a comparison can shed light on commonalities and/or differences between the  
 81 two rates and the underlying processes. Published data indicate that  $\theta$  values typically  
 82 vary between 0.35 – 0.7 [*Whipple and Tucker*, 1999; *Tucker and Whipple*, 2002], whereas  
 83  $p$  values span a wider range ( $p = -3, 0, 0.24, 0.33, 0.54, 1.125$ ; for *Mackey et al.* [2014];  
 84 *Weissel and Seidl* [1998]; *Haviv* [2007]; *DiBiase et al.* [2015]; *Berlin and Anderson* [2007];

85 *Crosby and Whipple* [2006], respectively). These published data, however, are hindered by  
86 the small number of reported  $p$  measurements and the general lack of uncertainty bounds  
87 for reported  $p$  and  $\theta$  values. Further,  $p$  and  $\theta$  values are often not measured over the  
88 same channel segments and, as far as we know, the covariance between them has not been  
89 explored.

90 In this study we compare  $p$  and  $\theta$  over the same channel sections while quantifying  
91 their uncertainty. We also explore the covariance between  $p$  and  $\theta$ , and the influence of  
92 various factors on  $p$ . To do so we use existing and new methods to compute  $p$ ,  $\theta$ , and  
93 their uncertainty from digital elevation models (DEMs) of 12 river basins with multiple  
94 waterfalls. Our analyses indicate that  $p$  and  $\theta$  are: (1) similar within uncertainty, (2)  
95 come from a similar distribution, and (3) generally covary. We also show that optimized  
96  $p$  values are sensitive to the variability in the basin area that drains to waterfalls, which  
97 could explain the wide range of  $p$  values that has been reported in the literature.

## 2. Method

98 To explore the similarity between  $p$  and  $\theta$  we analyze 12 natural basins with multiple  
99 waterfalls in different climatic and lithologic conditions (Table 1, Table S1). We first  
100 detect the location of waterfalls and the uncertainty in their location in a systematic  
101 manner (Section 2.2). We then use these locations and uncertainties to compute the  
102 optimal  $p$  and  $\theta$  values (Sections 2.3, 2.4), and their uncertainty (Section 2.5) for each of  
103 the analyzed basins. For consistency, we compute the values of  $\theta$  over the same channel  
104 sections used to compute  $p$  (i.e., between the waterfalls and a downstream location that  
105 drains all waterfalls). To verify that our results are consistent across methods for  $p$  and  $\theta$

106 computation, we use three different methods to compute  $\theta$  and two methods to compute  
107  $p$ . The resulting  $p$  and  $\theta$  values are then compared.

## 2.1. Study sites

108 We explored the values of  $p$  and  $\theta$  by analyzing basins with multiple waterfalls identified  
109 using a 1 arc-second SRTM DEM ( $\sim 30$  m for the studied basins) [Rodríguez *et al.*, 2005]  
110 (Table 1, Table S1). The basins were selected based on the following criteria: (1) multiple  
111 waterfalls (to effectively constrain  $p$ ); (2) waterfalls are clearly detectable over the DEM  
112 resolution (Section 2.2, Figures 1); (3) the drainage area at the waterfall ( $A_w$ ) in some  
113 of the selected basins spans a wide range of values such that in these cases it is unlikely  
114 that waterfall location can be explained solely via a drainage area threshold [i.e., Crosby  
115 and Whipple, 2006]; (4) basins span different precipitation regimes in order to explore the  
116 potential influence of precipitation on  $p$  and  $\theta$  [e.g., Zaprowski *et al.*, 2005] (Table 1).

## 2.2. Waterfall identification

117 We applied a quasi-automatic waterfall identification procedure to detect waterfalls in  
118 a repeatable and efficient manner (Figure 2). We first used the DEM to visually detect  
119 all potential waterfalls within a basin and extract the profiles of channel segments that  
120 contain waterfalls. For each segment we identified the waterfall location and its boundaries  
121 using the following procedure: (a) for each node along the channel segment we recorded  
122 elevation and drainage area ( $z_i$ ,  $A_i$ , where  $i$  is the node index); (b) the slope ( $S_i$ ) at each  
123 node was computed via a central difference scheme over a window of 9 nodes (a window  
124 size selected based on iterative experimentation) along the channel to suppress slope errors  
125 that propagate from elevation errors in the DEM [i.e., Wobus *et al.*, 2006a]; (c) Values of

126  $k_{sn}$  (normalized channel steepness index, [e.g., *Wobus et al.*, 2006a]) were computed for  
 127 each channel node utilising  $k_{sn_i} = S_i A_i^{0.5}$  (an exponent value of 0.5 is generally similar  
 128 to that computed for most basins we studied, and is in agreement with values that are  
 129 traditionally used); (d) waterfall location was detected by finding the node of highest  $k_{sn_i}$   
 130 where the slope across the waterfall also exceeds a prescribed threshold (0.2, in agreement  
 131 with the upper slope limit of step-pool and cascade reaches [*Montgomery et al.*, 1995;  
 132 *Montgomery and Buffington*, 1997] as well as lag-debris reaches beneath waterfalls [*Haviv*  
 133 *et al.*, 2010; *Haviv*, 2007]); (e) The top and bottom boundaries of the waterfall were  
 134 defined by progressing from the waterfall up- and down- stream until the first node where  
 135  $S_i$  is smaller than half of the prescribed knickpoint threshold (i.e.,  $< 0.1$ ). If  $S_i$  does not  
 136 decrease below this value; the channel is relatively steep so the waterfall is defined as not  
 137 being sufficiently distinguishable and is excluded from the analysis. These boundaries are  
 138 used as measures of uncertainty in waterfall location. We executed this routine over all  
 139 basins and visually confirmed the location of the selected waterfalls and their boundaries  
 140 (Figure 3).

## 2.3. Computation of $p$ value

### 141 2.3.1. Time based optimization of $p$

142 To compute  $p$  for each basin we used an optimization procedure that minimizes the  
 143 scatter in recession duration (i.e., the time-span of recession) among the observed water-  
 144 falls [e.g., *Brocard et al.*, 2016]. This procedure relies on a commonly used assumption  
 145 [e.g., *Weissel and Seidl*, 1998; *Crosby and Whipple*, 2006; *Berlin and Anderson*, 2007;  
 146 *Brocard et al.*, 2016] that all waterfalls initiated as a single waterfall that was located at  
 147 the trunk channel at some initial time  $t_s$ , and over the time period between  $t_s$  and the



148 present (hereafter recession duration) receded and bifurcated at tributary junctions to  
 149 their current location. We also assume that the waterfall recession rate is described by  
 150 equation (5) and that the value of  $B$  and  $p$  are uniform within the basin. These assump-  
 151 tions are similar to those used by other studies [*Crosby and Whipple, 2006; Berlin and*  
 152 *Anderson, 2007; Whittaker and Boulton, 2012; DiBiase et al., 2015; Brocard et al., 2016*].

153 The  $p$  value that optimizes the fit between modeled and natural waterfall locations  
 154 can be computed either from the spatial misfit between the location of modeled and  
 155 observed waterfalls [e.g., *Crosby and Whipple, 2006; Berlin and Anderson, 2007*], or from  
 156 the temporal misfit in arrival time of the modeled waterfall to the location of the observed  
 157 ones [e.g., *Brocard et al., 2016*]. We computed  $p$  through the latter approach that is most  
 158 consistent with the assumption that all waterfalls migrated to their current position over  
 159 the same time period. The recession duration (i.e., the time-span of recession) between  
 160 the initial waterfall location and the current one is cast as [following *Crosby and Whipple,*  
 161 *2006; Berlin and Anderson, 2007*]:

$$t_r(N_n) = \sum_{i=1}^{N_n} \Delta t_i = \sum_{i=1}^{N_n} \frac{\Delta x}{C_{ew,i}} \delta_i, \quad (6)$$

162 where  $N_n$  is the number of nodes between the initial waterfall location at  $t_s$  and the current  
 163 waterfall location,  $\Delta t_i$  [T] is the recession duration between nodes  $i$  and  $i + 1$ .  $C_{ew,i}$  [L/T]  
 164 is the waterfall celerity between nodes  $i$  and  $i + 1$  that is evaluated as  $BA_i^p$  (equation  
 165 (5)) where  $A_i$  is the drainage area of the  $i$ 'th node.  $\Delta x$  is the the distance between DEM  
 166 nodes in the cardinal directions, and  $\delta_i$  is a dimensionless variable that equals 1 or  $\sqrt{2}$  for  
 167 cardinal and diagonal flow direction between nodes  $i$  and  $i + 1$ , respectively.

168 To compute  $p$  in cases where the recession duration and initial waterfall location are un-  
 169 known, we non-dimensionalized the duration of waterfall recession to:  $t_r^*(N_n) = \sum_{i=1}^{N_n} \Delta t_i^*$ ,

170 where  $\Delta t_i^* = \Delta t_i / \Delta t_0$ . We set  $\Delta t_0 = \frac{\Delta x}{BA_0^p}$  where  $A_0$  is an arbitrary reference drainage  
 171 area. The non-dimensional recession duration is:

$$t_r(N_n)^* = \sum_{i=1}^{N_n} \Delta t_i^* = A_0^p \sum_{i=1}^{N_n} A_i^{-p} \delta_i. \quad (7)$$

172 We find the optimal  $p$  value while accounting for the uncertainty in waterfall positions.  
 173 To do so, we computed the dimensionless recession duration ( $t_r^*$ , equation (7)) between  
 174 the initial waterfall location and each of the observed waterfalls for each  $p$  value (from 0 to  
 175 2 in intervals of 0.01). We then calculated the weighted misfit ( $\chi_r^2$ ) in recession duration  
 176 between waterfalls:

$$\chi_r^2 = \frac{1}{N_p - 1} \sum_{i=1}^{N_p} \frac{D_i^2}{\sigma_i^2} = \frac{1}{N_p - 1} \sum_{i=1}^{N_p} \frac{t_{r,i}^* - \bar{t}_r^*}{\sigma_i^2}, \quad (8)$$

177 where  $N_p$  is the number of waterfalls,  $D_i$  is the difference in  $t_r^*$  between the  $i$ 'th waterfall  
 178 ( $t_{r,i}^*$ ) and the mean  $t_r^*$  for all waterfalls ( $\bar{t}_r^*$ ), and  $\sigma_i$  is a measure of uncertainty in recession  
 179 duration computed from the standard deviation of the nondimensional recession time to  
 180 the top and bottom boundaries of the  $i$ 'th waterfall (because this is a standard deviation  
 181 of two values only, it equals half of the difference in  $t_r^*$  between these top and bottom  
 182 boundaries). The best fit  $p$  value is the one that produces the lowest  $\chi_r^2$  value (Figure 4).  
 183 The method successfully recovered the correct  $p$  values from synthetic experiments where  
 184 waterfall locations were modeled with a prescribed  $p$  values.

185 As long as the initial location of the waterfall is at the trunk stream downstream of all  
 186 waterfalls, the optimization of  $p$  is insensitive to the exact initial location of the waterfall  
 187 and the duration of waterfall recession. This is because waterfall recession along a trunk  
 188 channel downstream of all waterfalls shifts  $t_r^*(N_n)$  by a constant value for all waterfalls.  
 189 Hence, the initial location of the waterfall can be prescribed at any arbitrary location in

190 the trunk channel without affecting the optimization results that rely on minimizing the  
 191 scatter in  $t_r^*(N_n)$  between all waterfalls. This facilitates finding the best fit  $p$  without  
 192 knowing the recession duration and the exact initial location of the waterfall.

193 The method described above differs from the time-based optimization of *Brocard et al.*  
 194 [2016] in that it is designed to compute  $p$  while accounting for the uncertainty in waterfall  
 195 location. To explore whether the  $p$  values produced by the time-based approach we used is  
 196 similar to that produced by the distance-based approach of *Crosby and Whipple* [2006] and  
 197 *Berlin and Anderson* [2007], we also developed a distance-based optimization procedure  
 198 that can recover  $p$  when both the duration of recession and the exact initial location of  
 199 the waterfalls are unknown. The  $p$  values produced by these two approaches are equal  
 200 within error (see SI).

### 201 **2.3.2. Optimization of $p$ with a critical area threshold**

202 To account for the possibility that waterfall recession is halted when the basin area that  
 203 drains to the waterfall is below a critical threshold ( $A_c$  [L<sup>2</sup>], *Crosby and Whipple* [2006])  
 204 we also computed the optimal  $p$  for:

$$C_{ew} = B(A - A_c)^p . \tag{9}$$

205 Under these conditions  $C_{ew} = 0$  when  $A_c \geq A$ . The  $A_c$  value for each basin was determined  
 206 as the minimum drainage area over all the waterfalls in the basin. The optimal  $p$  value is  
 207 found by minimizing  $\chi_r^2$  as explained in section 2.3 (equation (8)).

### 208 **2.4. Extraction of $\theta$ value**

209 We computed  $\theta$ , and the uncertainty associated with it, using slope-area ( $S - A$ ) [e.g.,  
*Hack*, 1973; *Whipple and Tucker*, 1999; *Wobus et al.*, 2006a], and  $\chi - z$  [e.g., *Royden et al.*,

210 2000; *Perron and Royden, 2012*] relations. For the latter we computed  $\theta$  for both linear  
 211 and non-linear  $\chi - z$  relations. The analysis is conducted on channel portions that extend  
 212 from the bottom boundary of waterfalls (i.e., Section 2.2) downstream to the mutual  
 213 junction where the initial waterfall is prescribed. Focusing on these channel portions  
 214 assures that  $p$  and  $\theta$  are computed and compared over the same set of flow-pathways.

#### 215 2.4.1. Compute $\theta$ from slope area relations

216 The value of  $\theta$  is reported as the slope of the least square linear regression between  
 217  $\log(S)$  and  $\log(A)$  [e.g., *Howard and Kerby, 1983; Whipple and Tucker, 1999; Dietrich*  
 218 *et al., 2003; Wobus et al., 2006a*] at the relevant channel portions. To reduce the influence  
 219 of the DEM elevation error on  $S$  [i.e., *Wobus et al., 2006a*] we computed  $S$  over vertical  
 220 increments of  $\Delta z \simeq 100$  m such that  $\frac{\Sigma_z}{\Delta z} \simeq 0.1$  (where  $\Sigma_z = 10$  m, is the 90% DEM  
 221 elevation error [*Rodríguez et al., 2005*]).

#### 222 2.4.2. Compute $\theta$ from $\chi - z$ relations

223 An alternate procedure for calculating  $\theta$  relies on a comparison between elevation ( $z$ )  
 224 and an integral quantity of drainage area ( $\chi$  [L]) [*Royden et al., 2000; Royden and Perron,*  
 225 *2013; Perron and Royden, 2012; Mudd et al., 2014; Willett et al., 2014; Goren et al., 2014*]:

$$\chi(l) = A_0^\theta \int_{l_b}^l A(l)^{-\theta} dl, \quad (10)$$

226 where  $A_0$  is a reference  $A$  value (we prescribed  $A_0 = 1000$  m<sup>2</sup>), and  $l$  and  $l_b$  measure the  
 227 distance along the stream at up and downstream locations, respectively.

228 In theory, a linear relation between  $\chi$  and  $z$  should occur when all the following condi-  
 229 tions are met [*Perron and Royden, 2012*]: (a) the channel network is at steady state; (b)  
 230 the channel steepness index ( $k_s = (U/K)^{1/n}$ ) is spatially uniform; (c)  $\theta$  is spatially uni-  
 231 form; (d) the channel incision processes are adequately described by equation (1). When

232 these assumptions hold, the integration of channel slope over the distance  $l - l_b$  along the  
 233 channel yields [*Perron and Royden, 2012; Willett et al., 2014; Shelef and Hilley, 2014*]:

$$\begin{aligned}
 z(l) &= z(l_b) + \int_{l_b}^l S(l) dl, \\
 &= z(l_b) + k_s \int_{l_b}^l A^{-\theta} dl, \\
 &= z(l_b) + k_s A_0^{-\theta} \chi(l).
 \end{aligned}
 \tag{11}$$

234 where  $z(l_b)$  is the  $z$  value at  $\chi = 0$ . equation (11) demonstrates that when  $\chi$  is calcu-  
 235 lated with a  $\theta$  value that is representative of the analyzed channel and under the above  
 236 assumptions, the relation between  $\chi(l)$  and  $z(l)$  is linear and  $k_s A_0^{-\theta}$  is the coefficient of  
 237 proportionality. This equation also implies that when  $\chi$  is computed for multiple tribu-  
 238 taries, and is integrated in the up-flow direction from a common point downstream, the  
 239 correct  $\theta$  value should not only linearize all the profiles in  $\chi - z$  space, but also collapse  
 240 all tributaries to a single line [*Perron and Royden, 2012*].

241 If the channels downstream of waterfalls are assumed to be at steady state, an optimal  $\theta$   
 242 can be identified through an iterative search for a value that minimizes the deviation from  
 243 a least square linear regression between  $\chi$  and  $z$  [*Perron and Royden, 2012; Royden and*  
 244 *Perron, 2013; Mudd et al., 2014*] downstream of waterfalls. We used a range of  $\theta$  values  
 245 (from 0 to 2 in intervals of 0.01) to compute  $\chi$  for each DEM node along tributaries  
 246 that extend from the prescribed initial waterfall location to the bottom of waterfalls. We  
 247 integrated  $\chi$  using the rectangle rule to better capture the discrete changes in  $\chi$  across  
 248 channel junction [*Mudd et al., 2014*]. For each  $\theta$  value, we computed the least square  
 249 linear regression between  $\chi$  and  $z$  and calculated the misfit between the data and the  
 250 linear model using equation (8) where  $D_i$  is the difference between the observed and

251 predicted elevation at the  $i$ 'th node,  $\sigma_i$  is the DEM vertical error (i.e., 10 m), and  $N_p$  is  
 252 the number of  $\chi - z$  pairs. The optimal  $\theta$  value minimizes the misfit (equation (8)).

253 Non-linear  $\chi - z$  relations may occur when temporally and/or spatially varying uplift,  
 254 climate, and rock properties affect the geometry of the channel network [e.g., *Royden and*  
 255 *Perron, 2013; Mudd et al., 2014; Goren et al., 2014*]. To acknowledge this possibility we  
 256 computed  $\theta$  through a binning approach [after *Goren et al., 2014*] that minimizes the  
 257 scatter of  $z$  values within each  $\chi$  bin with multiple tributaries, so that it does not force  
 258 the same linear relation over the entire  $\chi$  and  $z$  range. For each  $\theta$  value, the procedure  
 259 divides the range of  $\chi$  values to 100 bins (based on an iterative experiment that shows  
 260 that stable  $\theta$  values are attained with more than 20 bins), and computes equation (8) for  
 261 bins that contain more than one tributary. The optimal  $\theta$  value is that which minimizes  
 262 equation (8), where  $D_i$  is the standard deviation of  $z$  values within each bin, and  $\sigma_i$  is the  
 263 DEM vertical error (i.e., 10 m).

## 2.5. Uncertainty in $p$ and $\theta$

264 The values of  $p$  and  $\theta$  are often reported without a measure of uncertainty, thus inhibiting  
 265 a comparison that accounts for the uncertainty in each of these parameters. For  $\theta$  values  
 266 computed from the slope of the least square linear regression of  $\log(S)$  vs.  $\log(A)$  (Section  
 267 2.4.1), the uncertainty in  $\theta$  for each of the basins is reported as two standard deviations  
 268 of the computed slope [*Montgomery and Runger, 2010*]. For  $\theta$  values computed from  
 269  $\chi - z$  relations (Section 2.4.2), as well as for  $p$  values computed from  $t_r^*$  (Section 2.3), we  
 270 calculated the uncertainty for each basin through an iterative bootstrap approach that  
 271 repeatedly computes  $p$  (or  $\theta$ ) for subsets of the flow pathways in each basin. This is  
 272 executed for 50 iterations, where in each iteration we compute the optimal  $p$  (or  $\theta$ ) value

273 for an arbitrarily chosen subset of the flow pathways (Figure 4). We then compute the  
274 lower and upper uncertainty bounds in  $p$  (or  $\theta$ ) for each basin from the 2.5 and 97.5  
275 percentiles of the optimal  $p$  (or  $\theta$ ) values computed in these 50 iterations (Figure 4). In  
276 each iteration the number of flow pathways is the integer value closest to 75% of the total  
277 number of flow pathways.

### 3. Results

#### 3.1. Waterfalls, longitudinal profiles, and their characteristics

278 Figure 3 shows river longitudinal profiles along the analyzed basins. We find that  
279 the elevation of the waterfalls in each basin is generally similar within uncertainty (i.e.,  
280 the top and bottom boundaries of the waterfall, Figure 3). In some basins this ele-  
281 vation consistently changes with distance from the origin (e.g., Figure 3a-c,h), or is  
282 rather scattered (Figure 3f). Review of geologic maps (Table 1), air-photos, pictures  
283 (<https://www.google.com/earth/>, <http://www.panoramio.com>), and previous work [*Melis*  
284 *et al.*, 1996; *Ruiz*, 2002; *Weissel and Seidl*, 1997, 1998; *Berlin and Anderson*, 2007] sug-  
285 gests that in most of the analyzed basins the waterfalls occur over an erosion-resistant  
286 sedimentary layer.

#### 3.2. Computed $p$ values

287 Computed values of  $p$  typically span a range of 0.3-0.9 (Figures 5, Table S1). High values  
288 of  $p$  ( $\approx 1$ ) occur in basins a and k and are associated with a low standard deviation ( $\sigma_a$ ),  
289 and relative standard deviation ( $\sigma_a/\mu_a$ , where  $\mu_a$  is the mean drainage area at waterfalls)  
290 of the drainage area at waterfalls (Figure 5a). The uncertainty in  $p$  is sensitive to the  
291 number of waterfalls ( $N_p$ ) in the analyzed basin and suggests that this uncertainty stabi-

292 lizes when  $N_p \gtrsim 10$  (Figure 5b). Values of  $p$  computed through the time-based method  
 293 with and without a critical area threshold ( $A_c$ ) covary and are similar within uncertainty  
 294 (Figure 5c), where a model with  $A_c > 0$  typically produces lower  $p$  values compared to  
 295 a model with  $A_c = 0$ . Values of  $p$  do not display a clear covariance with precipitation,  
 296 waterfall height, or slope (Figure 5d-f, height and slope are measured between the top  
 297 and bottom waterfall boundaries). The  $\chi_r^2$  optimization curves (SI) tend to be better con-  
 298 strained for basins with large number of waterfalls (Table S1). The  $p$  value we computed  
 299 for basins e-j ( $0.49_{-0.05}^{+0.04}$ ,  $0.44_{-0.04}^{+0.28}$ ,  $0.39_{-0.03}^{+0.02}$ , respectively, computed with  $A_c = 0$ ) differs  
 300 from the  $p$  value estimated by *Weissel and Seidl* [1998] for the same catchment ( $p \sim 0$ ).  
 301 This deviation likely reflects differences in the DEM resolution, number of waterfalls, and  
 302 optimization technique. This study uses DEMs of 30 m resolution, 47 waterfalls, and the  
 303 aforementioned  $p$  optimization technique, whereas the study of *Weissel and Seidl* [1998]  
 304 used DEMs of 500 m resolution, 11 waterfalls, and visual approximation of  $p$ . Further, this  
 305 study analyzed each basin separately, whereas *Weissel and Seidl* [1998] analyzed basins  
 306 e-g together, starting approximately 150 km downstream of the confluence where these  
 307 basins join.. The  $p$  values computed for basins h and i, ( $0.51_{-0.1}^{+0.12}$ ,  $0.53_{-0.07}^{+0.06}$ , respectively,  
 308 computed with  $A_c = 0$ ) are similar to the value computed by *Berlin and Anderson* [2007]  
 309 for these two basins combined using a distance based-optimization ( $p = 0.54$ ).

### 3.3. Computed $\theta$ values

310 Computed values of channel concavity ( $\theta$ ) typically span a range of 0.3-0.7 (Figure 6,  
 311 Table S1). In contrast to  $p$ , the uncertainty in  $\theta$  is generally independent on the number  
 312 of waterfalls (Figure 6a), and  $\theta$  is generally insensitive to  $\sigma_a$  (Figure 6b).  $\theta$  does not show  
 313 a clear covariance with precipitation (Figure 6c). The  $\theta$  values computed through slope-



314 area relations somewhat deviate from those computed based on linear or binning based  
 315 optimization of  $\chi - z$  relations ( $\theta_{\chi-z-lin}$  and  $\theta_{\chi-z-bin}$ , respectively, Section 2.4, Figure 7).  
 316 In some basins the  $\chi - z$  relations for the flow pathways downslope of the waterfalls are  
 317 scattered and so are the slope area relations, suggesting that these basins deviate from  
 318 the linear relation expected when channels are at steady state and lithology and uplift are  
 319 spatially homogenous (SI).

### 3.4. Comparison of $\theta$ and $p$

320 Comparison of  $p$  and  $\theta$  shows that they are generally similar within uncertainty (Figure  
 321 7, Tables 1, S1). The optimal  $p$  and  $\theta$  values generally covary for basins of  $\gtrsim 10$  waterfalls,  
 322 Figure 7c). Least square linear regression between  $p$  computed with  $A_c = 0$  and  $\theta$  com-  
 323 puted through all the aforementioned methods produces  $\theta = 0.054(\pm 0.13) + 0.95(\pm 0.31)p$   
 324 (uncertainty is reported based on 95% confidence interval), with an  $R^2 = 0.64$ , and a  
 325 probability (p) value of  $2.4 \times 10^{-6}$ . Similar analysis for  $p$  computed with  $A_c > 0$  pro-  
 326 duces  $\theta = 0.006 + 1.19p$  with an  $R^2 = 0.59$  and a probability (p) value of  $1.2 \times 10^{-5}$ .  
 327 Note that in both cases the intercept is  $< 0.1$  and the slope is close to unity, suggesting  
 328 that  $p$  and  $\theta$  are generally similar. A ranked correlation produces a Kendall correlation  
 329 coefficient of 0.55 and a probability (p) value of  $4.4 \times 10^{-4}$ . The difference between  $p$   
 330 and  $\theta$  is maximal when  $p$  values are high (Figure 7a). A Kolmogorov-Smirnov test that  
 331 compared the distributions of  $p$  and  $\theta$  for all basins failed to reject the null hypotheses  
 332 that  $p$  and  $\theta$  are drawn from the same population. Similarly, a Wilcoxon signed rank test  
 333 that compared the paired (by basin) values of  $p$  and  $\theta$  failed to reject the null hypothesis  
 334 that the population of differences between  $p$  and  $\theta$  pairs comes from a distribution whose  
 335 median is zero. Note that in both of these tests the null hypothesis (i.e., similarity of  $p$

336 and  $\theta$ ) is not rejected despite the very conservative significance level used ( $\alpha = 0.5$ , an  
337 order of magnitude larger than the commonly used  $\alpha = 0.05$ ).

## 4. Discussion

### 4.1. Similarity between $p$ and $\theta$

338 The similarity between  $p$  and  $\theta$  is supported through multiple means of comparison.  
339 Whereas the similarity 'within uncertainty' (Figure 7a) may depend on how the uncer-  
340 tainty in  $p$  and  $\theta$  is computed, the statistical tests are more robust and suggest that the  
341 values of  $p$  and  $\theta$  are drawn from the same population (i.e., Kolmogorov-Smirnov test),  
342 and that when matched by a basin, neither  $p$  or  $\theta$  is consistently higher than the other (i.e.,  
343 Wilcoxon signed rank test). The covariance between  $p$  and  $\theta$  (for basins with 10 waterfalls  
344 or more), and their alignment along a  $\sim 1:1$  line further supports their similarity.

345 One interpretation of the similarity between  $p$  and  $\theta$  is that it stems from the functional  
346 similarity between  $t_r^*$  and  $\chi$  (Equations 7, 10), where both  $t_r^*$  and  $\chi$  at the waterfall can  
347 represent the duration of waterfall recession [e.g., *Whipple and Tucker, 1999; Perron and*  
348 *Royden, 2012; Goren et al., 2014*]. Conceptually, when all tributaries collapse to a single  
349 line in  $\chi - z$  space, and the waterfalls are of equal elevation, an equality of  $p$  and  $\theta$  is  
350 inevitable (Figure 8a, b). However, perfect alignment of  $\chi$  and  $z$  rarely occurs in natural  
351 settings, so that different values of  $p$  and  $\theta$  may occur. For example, Figures 8c and 8d,  
352 show a scenario where waterfalls are of equal elevation but the  $\theta$  value that minimizes  
353 the scatter in  $z$  for all  $\chi$  values along the channels (Figure 8c) differs from the  $p$  value  
354 that minimizes the scatter in  $t_r^*$  at the waterfalls only (Figure 8d). Similarly, Figures 8e,  
355 and 8f, show a scenario with a perfect alignment of  $\chi$  and  $z$  but waterfalls at different  
356 elevations, such that once again the  $\theta$  value that minimizes the scatter in  $z$  for all  $\chi$  values

357 (Figure 8e) differs from the  $p$  value that minimizes the scatter in  $t_r^*$  at the waterfalls only  
 358 (Figure 8f). These differences between  $p$  and  $\theta$  occur because  $p$  minimizes the scatter in  
 359  $t_r^*$  (or  $\chi$ ) at the waterfall location only, while  $\theta$  minimizes the scatter in  $z$  for  $\chi$  (or  $t_r^*$ )  
 360 values everywhere along the analyzed channels.

361 In most of the analyzed basins waterfalls are approximately at the same elevation (within  
 362 uncertainty, Figure 3). Whereas this can be interpreted as if the similarity between  $p$  and  
 363  $\theta$  stems from the idealized case described in Figure 8b, the lack of clear relations between  
 364 the spread in waterfall elevations and the difference between  $p$  and  $\theta$  (SI), as well as the  
 365 scattered  $\chi - z$  relation for the analyzed basins (SI) suggests that the setting described  
 366 in Figure 8b is unlikely. Given that the optimization of  $\theta$  assigns equal weighting to all  
 367 points along the channel profile, and that of  $p$  accounts for waterfall location only, the  
 368 similarity between  $p$  and  $\theta$  may capture commonalities between the processes that shape  
 369 the channel profile and those that determine the location of waterfalls.

#### 4.2. Potential process-based rationale for the similarity of $p$ and $\theta$

370 In the context of the channel incision law,  $p = \theta = m/n$  suggests that the exponent  
 371 value that describes the influence of drainage area ( $A$ ) on waterfall celerity is similar to  
 372 that which describes the influence of  $A$  on the celerity of non-vertical waterfalls (Section  
 373 1). This functional similarity may have several explanations.

374 A potential explanation for  $p = m/n$  is that waterfall celerity is primarily influenced by  
 375 water discharge and channel width, for which  $A^{m/n}$  is a proxy (i.e.,  $m/n = c(1 - b)$  where  
 376  $c$  and  $b$  are exponent relating drainage area to channel discharge and width, respectively,  
 377 *Whipple and Tucker [1999]*). For example, discharge can influence the retreat of a quasi  
 378 vertical waterfall face through plunge pool erosion, by shear on sub-vertical slabs which

379 will eventually topple, by removing and breaking boulders which can buttress the waterfall  
380 face, by supplying sediments that can enhance erosion, and by influencing wet-dry related  
381 weathering of the waterfall face. Since water velocity matters in all these processes, the  
382 width of the channel at a given discharge also matters. Hence, waterfall recession may  
383 be a function of  $A^{m/n}$ . Whereas multiple factors influence waterfall celerity (see Section  
384 1), many of these factors can covary with channel geometry and discharge, and therefore  
385 with  $A^{m/n}$ . Further exploration of the relations between these different factors and  $A^{m/n}$   
386 is needed to support this potential explanation, and to evaluate the relative influence of  
387 processes that do not depend on  $A$  on waterfall recession.

388 An alternate explanation for the similarity between  $p$  and  $m/n$  is that the recession of  
389 a waterfall, and that of downstream non-vertical channel segments are dependent. Such  
390 dependency was suggested by *Haviv et al.* [2010], who explored the recession of a waterfall  
391 with a resistant cap-rock underlain by a weaker sub-cap-rock. In that case, *Haviv et al.*  
392 [2010] demonstrated that a recession of a non-vertical channel segment downslope of a  
393 waterfall (driven by downstream incision) can result in increased waterfall height once the  
394 receding segment abuts against the waterfall (as long as the vertical incision rate below  
395 the waterfall is greater than that upstream of the waterfall). When the waterfall height  
396 reaches a threshold for gravitationally induced failure, the waterfall fails and recedes, the  
397 resulting debris is transported down the channel, and the process repeats (Figure 9).

398 A mechanism in which the waterfall celerity is dependent on (i.e., enslaved to) the celer-  
399 ity of the downstream channel segment requires that over long time-scales the waterfall  
400 celerity ( $C_{ew}$ ) equals the celerity of non-vertical channel segments ( $C_e$ ). In the context  
401 of Equations 3-5 this requires that the waterfall celerity coefficient ( $B$ ) equals the chan-

402 nel erodibility  $K$ . We are not aware of direct comparisons of these coefficients across  
403 basins with well defined waterfalls such as those explored in this study, however, the  $B$   
404 value computed by *Berlin and Anderson* [2007] for waterfalls in the Roan Plateau, CO  
405 ( $B = 1.37 \times 10^{-7} [\text{m}^{0.08}\text{yr}]^{-1}$ , computed with  $p = 0.54$ ) is within the range of empirically  
406 calibrated  $K$  values for models with  $0.5 \leq m/n \leq 0.59$  and  $n = 1$  [*Stock and Montgomery*,  
407 1999; *Ferrier et al.*, 2013; *Murphy et al.*, 2016]. However, a case where waterfall recession  
408 is faster than that imposed by channel incision downstream (i.e.,  $C_{ew} > C_e$ ) was shown by  
409 *DiBiase et al.* [2015] for the Big Tujunga Creek that is incised into the crystalline rocks of  
410 the San-Bernardino mountains, CA. The high recession rate of the Niagara falls [*Gilbert*,  
411 1907], for example, is also unlikely to be in balance with the recession imposed by channel  
412 incision (i.e., Figure 9) downstream. These examples suggest that the factors that govern  
413 waterfall recession may vary in time and space, and that a single mechanism is unlikely  
414 to explain the variety of observed phenomena. Direct comparison of  $K$ ,  $B$ ,  $p$ , and  $\theta$  in  
415 locations where erosion rate, as well as the duration and spatial extent of waterfalls retreat  
416 are well constrained, can reveal whether, and under what conditions, waterfall recession  
417 is enslaved to that of downstream channel segments (Figure 9).

### 4.3. Examination of assumptions

418 The assumption that all waterfalls initiated as a single waterfall at the trunk channel  
419 downstream of all waterfalls underlies our computation of  $p$ . Whereas we could not test  
420 for this assumption, such assumption was previously made for some of the analyzed basins  
421 [i.e., *Berlin and Anderson*, 2007; *Weissel and Seidl*, 1998], and is common in studies of  
422 waterfall and knickpoint propagation [e.g., *Crosby and Whipple*, 2006; *Brocard et al.*,  
423 2016; *DiBiase et al.*, 2015]. The occurrence of waterfalls over a sub-horizontal, erosion-

424 resistant layer that is underlain by a weaker layer supports this assumption. This is  
425 because it suggests that this layer is initially incised at a downstream location where it is  
426 first transected by the stream, and the resulting waterfall then propagates upstream.

427 A second assumption, that underlies our computation of  $p$ , is that the celerity coef-  
428 ficient,  $B$ , and the exponent  $p$ , are spatially constant along the analyzed channel sec-  
429 tions. Spatial homogeneity can stem from the spatial continuity of lithologic layers in  
430 many of the analyzed basins. This is suggested by geologic maps (Table 1), air-photos,  
431 pictures (<https://www.google.com/earth/>, <http://www.panoramio.com>), and published  
432 work [*Melis et al.*, 1996; *Ruiz*, 2002; *Berlin and Anderson*, 2007] that indicate that in  
433 most of the analyzed basins the channel system is incised into sub-horizontal lithologic  
434 layers, and waterfalls occur over spatially continuous erosion-resistant layers underlain by  
435 weaker layers (except for basins e-g where this varies spatially [*Weissel and Seidl*, 1998]  
436 and at least some of the waterfalls are composed of a series of small waterfalls). The  
437 horizontal continuity of these layers can facilitate spatial homogeneity in  $B$  and  $p$ , where  
438 waterfalls, as well as non-vertical channel segments downstream, everywhere recede over  
439 the same lithologic units [e.g., *Haviv et al.*, 2006; *Berlin and Anderson*, 2007; *Haviv*, 2007;  
440 *Haviv et al.*, 2010] (Figure 9). Observations concerning the stratigraphic position of wa-  
441 terfalls and whether their lower boundary is tied to a specific lithologic horizon can assist  
442 in evaluating the feasibility of stratigraphically controlled homogeneity.

443 The possibility that the similarity of  $p$  and  $\theta$  stems from enslavement of the waterfall  
444 celerity to that of the non-vertical channel downstream of the waterfall is underlain by  
445 few assumptions. First, this mechanism was suggested and explored for waterfalls over  
446 a resistant cap-rock underlain by a weaker sub-cap-rock [*Haviv et al.*, 2010] (this also

447 appears to be the case in most of the basins we analyzed), and may not be valid for  
448 waterfalls in different settings. Second, in the context of Equations 3-5 and  $p = \theta$  this  
449 mechanism requires that downstream channel recession is proportional to  $A^{m/n}$ , either  
450 because  $n = 1$  or because at the downstream channel segment denudation and uplift  
451 rates are approximately balanced (i.e., Section 1). Such a balance in the downstream  
452 channel segment is possible, despite the irregular channel profiles (Figure 3), because of  
453 the aforementioned lateral continuity of lithologic layers. In that case, where the spatial  
454 homogeneity of  $\theta$  relies on the lateral continuity of specific layers but the value of  $\theta$  is  
455 computed over the heterogeneous lithology of the entire channel system, it is assumed that  
456 this  $\theta$  value is representative of the value of  $\theta$  just downstream of the waterfall. In the  
457 context of the enslavement mechanism, if the latter assumptions hold so that denudation  
458 and uplift are balanced, the similarity between  $p$  and  $\theta$  is not necessarily indicative of  
459  $n = 1$ .

460 Finally, the comparison between  $p$  and  $\theta$  and its interpretation from a process perspec-  
461 tive assumes that the underlying equations (i.e., Equations 2, 5) adequately describe the  
462 recession process. Whereas both equations were explored numerically and calibrated to  
463 field data [e.g., *Rosenbloom and Anderson, 1994; Bishop et al., 2005; Crosby and Whipple,*  
464 *2006; Whittaker and Boulton, 2012; Brocard et al., 2016*], alternate or more complicated  
465 models can perform equally well or better [e.g., *Crosby and Whipple, 2006; Lague, 2014*].  
466 A wide spread of  $p$  values, or a clear indication that an important process is overlooked  
467 by equation (5) can raise doubts concerning the validity of this equation. Our results,  
468 pointing at a general consistency in the value of  $p$  between basins, as well as at a similarity  
469 between  $p$  and  $\theta$ , suggest that Equations 2 and 5 do capture aspects of the recession pro-

cess that are consistent across the analyzed basins. This consistency lends some further support to the validity of these equations.

#### 4.4. The sensitivity of $p$ to basin properties and DEM resolution

The uncertainty in  $p$  is sensitive to the number of waterfalls ( $N_p$ ) within a basin (Figure 5b). In the context of our methodology for computing  $p$ , this suggests that when the number of waterfalls is small ( $N_p \lesssim 10$ , Figure 5b), the influence of each of the flow pathways selected in a bootstrap iteration is large, such that a variety of optimal  $p$  values can be produced depending on the selected subset. Our analyses therefore suggest that studies that aim to extract reliable  $p$  values with the methodology we used should focus on basins with a large number of waterfalls ( $N_p \gtrsim 10$ , Figure 5b).

The association between the exceptionally high  $p$  value ( $p \sim 1$ ) of basins a and k ( $0.94_{-0.12}^{+0.21}$ ,  $0.88_{-0.34}^{+0.24}$ , respectively, for a model with  $A_c = 0$ ), and the low variability in waterfalls drainage area ( $A_w$ ) that characterize these basins ( $\sigma_a \sim 10^6$  m<sup>2</sup>,  $\sigma_a/\mu_a < 0.5$ , Figure 5a), points at a potential dependency between these parameters. Note that basin d is associated with a low  $p$  despite a low standard deviation in  $A_w$  ( $\sigma_a$ ), yet this basin is associated with the lowest mean  $A_w$  ( $\mu_a$ ) of all basins ( $\sim 2 \times 10^6$  m<sup>2</sup>, Table S1), such that its relative standard deviation (i.e.,  $\sigma_a/\mu_a$ ) is higher than that of basins a and k. A dependency between  $p$  and the variability in  $A_w$  is aligned with the findings of *Crosby and Whipple* [2006], who computed high  $p$  value ( $p = 1.125$ ) for a basin with low variability in  $A_w$ .

Occurrence of high  $p$  values is predicted for equation (5) when waterfalls drain a similar drainage area (i.e., low variability in  $A_w$ , Figures 1, 5a) but have different distributions of drainage area ( $A$ ) along the down-stream flow pathway. These high  $p$  values occur because



492 waterfalls that drain similar drainage areas (i.e., small  $\sigma_a$ ) likely have similar  $A$  values  
493 along the channel just downstream of the waterfall, while further downstream along the  
494 waterfall migration pathway (and yet upstream of where flow pathways merge next to the  
495 initial waterfall location) values of  $A$  differ due to variations in the network topology. In  
496 that case, a high  $p$  is preferred by the optimization procedure because it increases the  
497 similarity in recession duration ( $t_r^*$ ) by heavily weighting the low  $A$  portion of the channel  
498 just downstream of the waterfall where the values of  $A$  are similar among channels (i.e.,  
499 equation (7)). As  $\sigma_a$  increases, lower  $p$  values are favored because they preferably weight  
500 the identical high  $A$  portion of channels downstream of large confluences where channels  
501 merge. This topologic argument suggests that high  $p$  values will be associated with low  
502 values of  $\sigma_a$ .

503 To explore this prediction, we run multiple  $p$ -optimization experiments where we used  
504 the topology (i.e., drainage area as a function of distance along the channels) for basin g,  
505 and imposed randomly positioned waterfalls within this basin topology. An initial set of  
506  $N_{s1}$  waterfall locations, constrained by a prescribed range of drainage area, was randomly  
507 selected from all possible locations for basin g. From this initial set we excluded all  
508 waterfall locations that have other waterfalls draining to them. From this screened subset  
509 of random locations we then randomly selected a prescribed number of waterfalls ( $N_{s2}$ )  
510 and used it to optimize  $p$ . To test the sensitivity of  $p$  to  $\sigma_a$  in this synthetic situation, the  
511 dependent variable was  $\sigma_a$ , namely, the permissible range of drainage areas from which the  
512  $N_{s1}$  locations are selected while maintaining the mean value of  $A_w$  ( $\mu_a$ ) approximately the  
513 same. We conducted 500 experiments with arbitrarily located waterfalls ( $N_{s1} = 20$ ,  $N_{s2} =$   
514 11). In each experiment we recorded the standard deviation of  $A_w$  ( $\sigma_a$ ), as well as the

515 relative standard deviation ( $\sigma_a/\mu_a$ ) and optimal  $p$  value. The results of this experiment  
516 show that a high value of  $p$  is indeed associated with low  $\sigma_a$ . As  $\sigma_a$  increases, the value of  
517  $p$  first declines steeply and then more gradually reaching approximately  $p = 0.5$  at higher  
518  $\sigma_a$  values (Figure 10).

519 The interpretation of  $p$  values computed for low  $\sigma_a$  should also account for the potential  
520 influence of DEM resolution. For example, waterfalls within the same basin may retreat  
521 according to equation (5) with a  $p$  value of 0.5 up to the upper reaches of the basin, where  
522 the area that drains to waterfalls ( $A_w$ ) decreases and so does the waterfall celerity. When  
523 mapped over a low resolution DEM, all waterfalls may appear to have the same  $A_w$  so  
524 the optimization procedure will prefer a higher value of  $p$ . In contrast, when mapped over  
525 high resolution DEM, small differences in  $A_w$  will become apparent so  $p = 0.5$  can be  
526 recovered. Hence, DEMs of higher resolution will allow more accurate recovery of  $p$ , and  
527 for a given resolution,  $p$  values computed for basins with high  $\sigma_a$  are likely more reliable.

528 For high values of  $\sigma_a$  the optimal  $p$  value for the synthetic experiments with arbitrary  
529 waterfall locations is in the range that is typical of  $\theta$  (Figure 10). This can be interpreted  
530 as if the similarity between  $p$  and  $\theta$  is insensitive to the exact location of waterfalls, and  
531 that  $p$  can be predicted from  $\sigma_a$  (SI). However, the covariance between  $p$  and  $\theta$  for basins  
532 of  $\geq 10$  waterfalls (Figure 7c), together with the low covariance between  $\theta$  and  $\sigma_a$  (Figure  
533 6c) suggests that the natural location of waterfalls is associated with significant subtleties  
534 in the value of  $p$  that reflect differences in the underlying process.

## 5. Summary

535 This study explores the similarity between channel profile concavity (i.e., the exponent  
536  $\theta$ ) downstream of waterfalls, and the exponent  $p$  that is used to model waterfall recession.

537 We analyzed channel profiles and the locations of waterfalls at 12 basins with different  
538 climatic and lithologic conditions, and also developed a new method to compute the  
539 optimal value of  $p$  and its uncertainty. Our results demonstrate that the values of  $p$  and  
540  $\theta$  are similar within uncertainty, come from a similar population, and generally covary for  
541 basins with  $\gtrsim 10$  waterfalls. In the context of the channel incision models this suggests  
542 that in the basins we analyzed waterfall recession is influenced by channel discharge and  
543 width as approximated by  $A^{m/n}$ , and/or that the waterfall celerity is enslaved to that of  
544 downstream channel segments.

545 Deviations between  $p$  and  $\theta$  primarily arise when  $p$  values are relatively high due to  
546 low variability in the area that drains to waterfalls, or to high uncertainty in  $p$ . This  
547 may occur when waterfall recession decreases at low  $A$  values and the DEM resolution  
548 is relatively low, or when the number of of waterfalls in a basin is  $< 10$ . To avoid these  
549 influences, we recommend that  $p$  values be computed over basins with a relatively large  
550 spread in  $A_w$  (i.e  $\sigma_a/\mu_a > 1$ ) and large number of waterfalls ( $> 10$ ).

551 Future studies focused on the relations between the waterfall celerity coefficient ( $B$ )  
552 and the channel erodibility coefficient ( $K$ ) may reveal whether, and for what conditions,  
553 waterfall celerity is similar to that of non-vertical channel segments. Such similarity would  
554 suggest that waterfall recession is enslaved to that of downstream segments. Furthermore,  
555 similarity would mean that landscape evolution models that implement the stream power  
556 or shear stress incision models are also suitable for simulating landscape evolution in the  
557 presence of waterfalls.

## 558 Notation

559  $A$  drainage area [ $L^2$ ]

- 560  $A_0$  reference drainage area [ $L^2$ ]
- 561  $A_c$  critical drainage area threshold [ $L^2$ ]
- 562  $A_i$  drainage area at a node  $i$  [ $L^2$ ]
- 563  $A_w$  area that drains to a waterfall [ $L^2$ ]
- 564  $A_r$  normalized drainage area used for plotting []
- 565  $B$  waterfall celerity coefficient [ $L^{1-2p}/T$ ]
- 566  $b$  exponent that relates drainage area to channel width []
- 567  $C_e$  knickpoint celerity [ $L/T$ ]
- 568  $C_{ew}$  waterfall celerity [ $L/T$ ]
- 569  $C_{ew,i}$  the waterfall celerity between nodes  $i$  and  $i + 1$  [ $L/T$ ]
- 570  $c$  exponent that relates drainage area to channel discharge []
- 571  $D_i$  measure of difference used in computing  $\chi_r^2$ , units vary with model
- 572  $E$  erosion rate [ $L/T$ ]
- 573  $i$  index of nodes []
- 574  $K$  erodibility coefficient in channel incision law [ $L^{1-2m}/T$ ]
- 575  $k_s$  channel steepness [ $L^{2m/n}$ ]
- 576  $k_{sn}$  normalized channel steepness [ $L^{2m/n}$ ]
- 577  $k_{sn_i}$  normalized channel steepness at a node  $i$  [ $L^{2m/n}$ ]
- 578  $l$  along stream flow distance up flow from  $l_b$  [ $L$ ]
- 579  $l_b$  along stream flow distance up flow from an arbitrary location [ $L$ ]
- 580  $m$  drainage area exponent in channel incision model []
- 581  $N_n$  number of nodes between the initial waterfall location at  $t_s$  and some upstream node
- 582 []

- 583  $N_p$  number of data points used in computing  $\chi_r^2$  []
- 584  $N_{s1}$  number of potential waterfall locations in a random selection process []
- 585  $N_{s2}$  number of waterfalls selected from a subset of randomly positioned waterfalls that  
586 do not drain to each other []
- 587  $n$  slope exponent in channel incision model []
- 588  $p$  drainage area exponent in posited waterfall celerity model []
- 589  $S$  channel slope []
- 590  $S_i$  slope at a node  $i$  []
- 591  $t_r$  duration of waterfall recession [T]
- 592  $t_r^*$  non dimensional duration of waterfall recession []
- 593  $\bar{t}_r^*$  mean non dimensional duration of waterfall recession for all waterfalls in a basin[]
- 594  $t_s$  time of initial waterfall formation [T]
- 595  $U$  uplift rate [L/T]
- 596  $U_n$  new uplift rate that is higher than the initial one[L/T]
- 597  $z$  elevation [L]
- 598  $z_i$  elevation at a node  $i$  [L]
- 599  $\alpha$  statistical significance level []
- 600  $\delta_i$  dimensionless variable that equals 1 or  $\sqrt{2}$  for cardinal and diagonal flow direction  
601 between nodes  $i$  and  $i + 1$ , respectively []
- 602  $\delta t$  small time increment [T]
- 603  $\Delta t_0$  reference waterfall recession duration [T]
- 604  $\Delta t_i$  recession duration between nodes  $i$  and  $i + 1$  [T]
- 605  $\Delta t_i^*$  non dimensional waterfall recession duration []

- 606  $\Delta x$  distance between DEM nodes in the cardinal directions [L]
- 607  $\mu_a$  mean of  $A_w$  in a basin [L<sup>2</sup>]
- 608  $\mu_z$  mean of waterfall elevation in a basin [L]
- 609  $\theta$  the ratio between the exponents  $m$  and  $n$  in the channel incision model []
- 610  $\theta_{SA}$  the value of  $\theta$  computed from the  $\log(A)$  vs.  $\log(S)$  []
- 611  $\theta_{\chi-z}$  the value of  $\theta$  computed from  $\chi - z$  relations []
- 612  $\theta_{\chi-z-lin}$  the value of  $\theta$  computed from linear  $\chi - z$  relations []
- 613  $\theta_{\chi-z-bin}$  the value of  $\theta$  computed from binned  $\chi - z$  relations []
- 614  $\sigma_i$  measure of uncertainty used in computing  $\chi_r^2$ , units vary with model
- 615  $\sigma_a$  standard deviation of  $A_w$  in a basin [L<sup>2</sup>]
- 616  $\sigma_z$  standard deviation of waterfall elevation in a basin [L]
- 617  $\Sigma_z$  vertical uncertainty in DEM [L]
- 618  $\chi$  transformation variable that links channel drainage area and length to elevation [L]
- 619  $\chi_r^2$  measure of weighted misfit in recession duration []

620 **Acknowledgments.**

621 Data supporting our analysis is contained as tables and figures within the manuscript and  
 622 supplements. We thank Joel Johnson, and two anonymous reviewers for constructive and  
 623 insightful comments that helped improve this manuscript. We are particularly thankful to  
 624 Joel Scheingross for insightful and thorough review. E.S. thanks S. Willett and S. Gallen  
 625 for constructive discussions regarding the impact of waterfalls on landscape evolution.

## References

- 626 Bagnold, R. (1966), An approach to the sediment transport problem from general physics,  
627 *U.S. Geological Survey Professional Paper 422-1*.
- 628 Berlin, M. M., and R. S. Anderson (2007), Modeling of knickpoint retreat on the Roan  
629 Plateau, western Colorado, *Journal of Geophysical Research: Earth Surface*, 112(F3),  
630 doi:10.1029/2006JF000553.
- 631 Bishop, P., T. B. Hoey, J. D. Jansen, and I. L. Artza (2005), Knickpoint recession rate and  
632 catchment area: the case of uplifted rivers in Eastern Scotland, *Earth Surface Processes  
633 and Landforms*, 30(6), 767–778, doi:10.1002/esp.1191.
- 634 Brocard, G. Y., J. K. Willenbring, T. E. Miller, and F. N. Scatena (2016), Relict landscape  
635 resistance to dissection by upstream migrating knickpoints, *Journal of Geophysical Re-  
636 search: Earth Surface*, 121(6), 1182–1203, doi:10.1002/2015JF003678.
- 637 Crosby, B. T., and K. X. Whipple (2006), Knickpoint initiation and distribution within  
638 fluvial networks: 236 waterfalls in the Waipaoa River, North Island, New Zealand,  
639 *Geomorphology*, 82(1), 16–38, doi:10.1016/j.geomorph.2005.08.023.
- 640 DiBiase, R. A., K. X. Whipple, M. P. Lamb, and A. M. Heimsath (2015), The role of  
641 waterfalls and knickzones in controlling the style and pace of landscape adjustment in  
642 the western San Gabriel Mountains, California, *Geological Society of America Bulletin*,  
643 127(3-4), 539–559, doi:10.1130/B311113.1.
- 644 Dietrich, W. E., D. G. Bellugi, L. S. Sklar, J. D. Stock, A. M. Heimsath, and J. J. Roering  
645 (2003), Geomorphic transport laws for predicting landscape form and dynamics, in *Pre-  
646 diction in Geomorphology, Geophysical Monograph Series*, vol. 135, edited by P. Wilcock  
647 and R. Iverson, pp. 103–132, AGU, Washington, D. C., doi:10.1029/135GM09.

- 648 Ferrier, K. L., K. L. Huppert, and J. T. Perron (2013), Climatic control of bedrock river  
649 incision, *Nature*, *496*(7444), 206–209, doi:10.1038/nature11982.
- 650 Gasparini, N. M., R. L. Bras, and K. X. Whipple (2006), Numerical modeling of non-  
651 steady-state river profile evolution using a sediment-flux-dependent incision model, *SD*  
652 *Willett et al., Geological Society of America Special Papers*, *398*, 127–141, doi:10.1130/  
653 2006.2398(04).
- 654 Gilbert, G. K. (1907), Rate of recession of niagara falls, *U.S. Geological Survey Bulletin*,  
655 *306*, 1–31.
- 656 Goren, L. (2016), A theoretical model for fluvial channel response time during time-  
657 dependent climatic and tectonic forcing and its inverse applications, *Geophysical Re-*  
658 *search Letters*, *43*(20), 10–753, doi:10.1002/2016GL070451.
- 659 Goren, L., M. Fox, and S. D. Willett (2014), Tectonics from fluvial topography using for-  
660 mal linear inversion: Theory and applications to the Inyo Mountains, California, *Journal*  
661 *of Geophysical Research: Earth Surface*, *119*(8), 1651–1681, doi:10.1002/2014JF003079.
- 662 Hack, J. T. (1973), Stream-profile analysis and stream-gradient index, *Journal of Research*  
663 *of the US Geological Survey*, *1*(4), 421–429.
- 664 Hail Jr, W. J. (1992), Geology of the central Roan Plateau area, northwestern Colorado,  
665 *U.S. Geological Survey Bulletin*, *1787-R*, 26p.
- 666 Haviv, I. (2007), Mechanics, morphology and evolution of vertical knickpoints (waterfalls)  
667 along the bedrock channels of the Dead Sea western tectonic escarpment., Ph.D. thesis,  
668 Hebrew University of Jerusalem, Israel.
- 669 Haviv, I., Y. Enzel, K. Whipple, E. Zilberman, J. Stone, A. Matmon, and L. Fifield  
670 (2006), Amplified erosion above waterfalls and oversteepened bedrock reaches, *Journal*



- 671 *of Geophysical Research: Earth Surface*, 111(F4), doi:10.1029/2006JF000461.
- 672 Haviv, I., Y. Enzel, K. Whipple, E. Zilberman, A. Matmon, J. Stone, and K. Fifield  
673 (2010), Evolution of vertical knickpoints (waterfalls) with resistant caprock: Insights  
674 from numerical modeling, *Journal of Geophysical Research: Earth Surface*, 115(F3),  
675 doi:10.1029/2008JF001187.
- 676 Howard, A. D., and G. Kerby (1983), Channel changes in badlands, *Geological Society  
677 of America Bulletin*, 94(6), 739–752, doi:10.1130/0016-7606(1983)943C739:CCIB3E2.  
678 0.CO;2.
- 679 Howard, A. D., and R. Kochel (1988), Introduction to cuesta landforms and sapping  
680 processes on the Colorado Plateau, in *Sapping Features of the Colorado Plateau: A  
681 Comparative Planetary Geology Field Guide*, vol. 491, p. 6, Scientific and Technical  
682 Information Office, National Aeronautics and Space Administration, Springfield, Va.
- 683 Lague, D. (2014), The stream power river incision model: evidence, theory and beyond,  
684 *Earth Surface Processes and Landforms*, 39(1), 38–61, doi:10.1002/esp.3462.
- 685 Lamb, M. P., A. D. Howard, J. Johnson, K. X. Whipple, W. E. Dietrich, and J. T. Perron  
686 (2006), Can springs cut canyons into rock?, *Journal of Geophysical Research: Planets*,  
687 111(E7), doi:10.1029/2005JE002663.
- 688 Lamb, M. P., A. D. Howard, W. E. Dietrich, and J. T. Perron (2007), Formation of  
689 amphitheater-headed valleys by waterfall erosion after large-scale slumping on Hawaii,  
690 *Geological Society of America Bulletin*, 119(7-8), 805–822, doi:10.1130/B25986.1.
- 691 Lamb, M. P., B. H. Mackey, and K. A. Farley (2014), Amphitheater-headed canyons  
692 formed by megaflooding at Malad Gorge, Idaho, *Proceedings of the National Academy  
693 of Sciences*, 111(1), 57–62, doi:10.1073/pnas.1312251111.

- 694 Mackey, B. H., J. S. Scheingross, M. P. Lamb, and K. A. Farley (2014), Knickpoint  
695 formation, rapid propagation, and landscape response following coastal cliff retreat at  
696 the last interglacial sea-level highstand: Kaua'i, Hawai'i, *Geological Society of America*  
697 *Bulletin*, 126(7-8), 925–942, doi:10.1130/B30930.1.
- 698 Mason, P. J., and K. Arumugam (1985), Free jet scour below dams and flip buckets,  
699 *Journal of Hydraulic Engineering*, 111(2), 220–235.
- 700 Melis, T. S., W. M. Phillips, R. H. Webb, and D. J. Bills (1996), When the blue-green  
701 waters turn red: Historical flooding in Havasu Creek, Arizona, *US Geological Survey*  
702 *water-resources investigations report*, pp. 96–4059.
- 703 Montgomery, D. C., and G. C. Runger (2010), *Applied statistics and probability for engi-*  
704 *neers*, John Wiley & Sons, New York.
- 705 Montgomery, D. R., and J. M. Buffington (1997), Channel-reach morphology in mountain  
706 drainage basins, *Geological Society of America Bulletin*, 109(5), 596–611, doi:10.1130/  
707 0016-7606(1997)109<0596:CRMIMD>2.3.CO;2.
- 708 Montgomery, D. R., J. M. Buffington, R. D. Smith, K. M. Schmidt, and G. Pess (1995),  
709 Pool spacing in forest channels, *Water Resources Research*, 31(4), 1097–1105, doi:10.  
710 1029/94WR03285.
- 711 Moon, S., C. P. Chamberlain, K. Blisniuk, N. Levine, D. H. Rood, and G. E. Hilley  
712 (2011), Climatic control of denudation in the deglaciated landscape of the Washington  
713 Cascades, *Nature Geoscience*, 4(7), 469–473, doi:10.1038/ngeo1159.
- 714 Mudd, S. M., M. Attal, D. T. Milodowski, S. W. Grieve, and D. A. Valters (2014),  
715 A statistical framework to quantify spatial variation in channel gradients using the  
716 integral method of channel profile analysis, *Journal of Geophysical Research: Earth*

- 717 *Surface*, 119(2), 138–152, doi:10.1002/2013JF002981.
- 718 Murphy, B. P., J. P. Johnson, N. M. Gasparini, and L. S. Sklar (2016), Chemical weather-  
719 ing as a mechanism for the climatic control of bedrock river incision, *Nature*, 532(7598),  
720 223–227, doi:10.1038/nature17449.
- 721 Niemann, J. D., N. M. Gasparini, G. E. Tucker, and R. L. Bras (2001), A quantitative  
722 evaluation of Playfair’s law and its use in testing long-term stream erosion models, *Earth*  
723 *Surface Processes and Landforms*, 26(12), 1317–1332, doi:10.1002/esp.272.
- 724 Perron, J. T., and L. Royden (2012), An integral approach to bedrock river profile analysis,  
725 *Earth Surface Processes and Landforms*, 38, doi:10.1002/esp.3302.
- 726 Rodríguez, E., C. Morris, J. Belz, E. Chapin, J. Martin, W. Daffer, and S. Hensley  
727 (2005), An assessment of the SRTM topographic products, *Tech. rep.*, JPL D-31639,  
728 Jet Propulsion Laboratory, Pasadena, California.
- 729 Rosenbloom, N. A., and R. S. Anderson (1994), Hillslope and channel evolution in a  
730 marine terraced landscape, Santa Cruz, California, *Journal of Geophysical Research:*  
731 *Solid Earth*, 99(B7), 14,013–14,029, doi:10.1029/94JB00048.
- 732 Royden, L., and T. J. Perron (2013), Solutions of the stream power equation and appli-  
733 cation to the evolution of river longitudinal profiles, *Journal of Geophysical Research:*  
734 *Earth Surface*, 118(2), 497–518, doi:10.1002/jgrf.20031.
- 735 Royden, L., M. Clark, and K. Whipple (2000), Evolution of river elevation profiles by  
736 bedrock incision: Analytical solutions for transient river profiles related to changing  
737 uplift and precipitation rates, *Eos Trans. AGU*, 81, 48.
- 738 Ruiz, G. M. H. (2002), Exhumation of the northern Sub-Andean Zone of Ecuador and its  
739 source regions, Ph.D. thesis, Diss., Naturwissenschaften ETH Zürich, Nr. 14905, 2003.

- 740 Scheingross, J. S., and M. P. Lamb (2016), Sediment transport through self-adjusting,  
741 bedrock-walled waterfall plunge pools, *Journal of Geophysical Research: Earth Surface*,  
742 doi:10.1002/2015JF003620.
- 743 Scheingross, J. S., D. Y. Lo, and M. P. Lamb (2017), Self-formed waterfall plunge  
744 pools in homogeneous rock, *Geophysical Research Letters*, *44*(1), 200–208, doi:10.1002/  
745 2016GL071730.
- 746 Seidl, M., and W. Dietrich (1992), The problem of channel erosion into bedrock, in *Func-*  
747 *tional Geomorphology: Landform Analysis and Models: festschrift for Frank Ahnert*, vol.  
748 Catena Supplement 23, edited by K. Schmidt and J. de Ploey, pp. 101–124, Cremlingen,  
749 Germany, Catena Verlag.
- 750 Shelef, E., and G. E. Hilley (2014), Symmetry, randomness, and process in the structure  
751 of branched channel networks, *Geophysical Research Letters*, *41*(10), 3485–3493, doi:  
752 10.1002/2014GL059816.
- 753 Stock, J. D., and D. R. Montgomery (1999), Geologic constraints on bedrock river incision  
754 using the stream power law, *Journal of Geophysical Research. B*, *104*, 4983–4993, doi:  
755 10.1029/98JB0213.
- 756 Tucker, G., and G. Hancock (2010), Modeling landscape evolution, *Earth Surface Pro-*  
757 *cesses and Landforms*, *35*(1), 28–50, doi:10.1002/esp.1952.
- 758 Tucker, G., and K. Whipple (2002), Topographic outcomes predicted by stream erosion  
759 models: Sensitivity analysis and intermodel comparison, *Journal of Geophysical Re-*  
760 *search: Solid Earth*, *107*(B9), doi:10.1029/2001JB000162.
- 761 Weissel, J. K., and M. A. Seidl (1997), Influence of rock strength properties on es-  
762 carpment retreat across passive continental margins, *Geology*, *25*(7), 631–634, doi:

- 763 10.1130/0091-7613(1997)025<0631:IORSPO>2.3.CO;2.
- 764 Weissel, J. K., and M. A. Seidl (1998), Inland propagation of erosional escarpments and  
765 river profile evolution across the southeast Australian passive continental margin, *Rivers*  
766 *over rock: fluvial processes in bedrock channels*, pp. 189–206.
- 767 Whipple, K., and G. Tucker (1999), Dynamics of the stream-power river incision model:  
768 Implications for height limits of mountain ranges, landscape response timescales, and  
769 research needs, *Journal of Geophysical Research*, *104*, 17,661–17,674, doi:10.1029/  
770 1999JB900120.
- 771 Whittaker, A. C., and S. J. Boulton (2012), Tectonic and climatic controls on knickpoint  
772 retreat rates and landscape response times, *Journal of Geophysical Research: Earth*  
773 *Surface*, *117*(F2), doi:10.1029/2011JF002157.
- 774 Willett, S. D., S. W. McCoy, J. T. Perron, L. Goren, and C.-Y. Chen (2014), Dynamic re-  
775 organization of river basins, *Science*, *343*(6175), 1248,765, doi:10.1126/science.1248765.
- 776 Wobus, C., K. X. Whipple, E. Kirby, N. Snyder, J. Johnson, K. Spyropolou, B. Crosby,  
777 and D. Sheehan (2006a), Tectonics from topography: Procedures, promise, and pitfalls,  
778 *Geological Society of America Special Papers*, *398*, 55–74, doi:10.1130/2006.2398(04).
- 779 Wobus, C. W., B. T. Crosby, and K. X. Whipple (2006b), Hanging valleys in fluvial  
780 systems: Controls on occurrence and implications for landscape evolution, *Journal of*  
781 *Geophysical Research: Earth Surface*, *111*(F2), doi:10.1029/2005JF000406.
- 782 Zaprowski, B. J., F. J. Pazzaglia, and E. B. Evenson (2005), Climatic influences on profile  
783 concavity and river incision, *Journal of Geophysical Research: Earth Surface*, *110*(F3),  
784 doi:10.1029/2004JF000138.

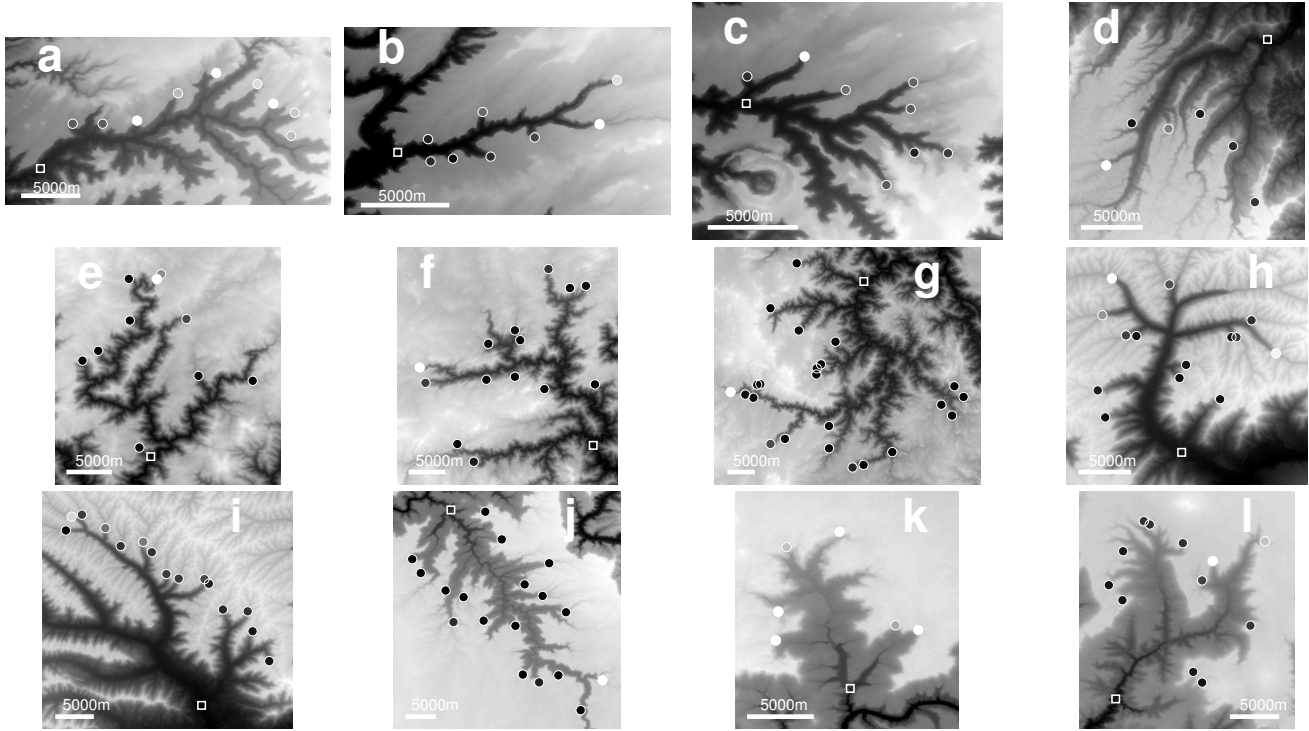


Figure 1: DEMs of the 12 basins analyzed in this study. Panels are labeled in accordance with the basin ID in Tables 1 and S1, where more information is provided regarding the location and characteristics of the different basins. Maps are shown in north to the top orientation and lighter colors represent higher elevation. Circles show the location of waterfalls and a white square shows the prescribed location of the initial waterfall for each basin. Circles are colored by relative drainage area at a waterfall within each basin ( $A_r = \frac{A_w}{\text{mean}(A_w)}$ , where light colors indicate high  $A_r$ , and  $A_w$  is the drainage area at the waterfall) to illustrate the scatter in drainage area at waterfalls. Note that waterfalls in basins a and k have lower variation in  $A_r$  values compared to other basins where some of waterfalls are associated with very high  $A_r$  values (light color), while others with very low (dark color). Basin locations are: a-c: Utah, USA, d: Pastaza, Ecuador, e-g: New South Wales, Australia, h-i: Colorado, USA, j-l: Arizona, USA.

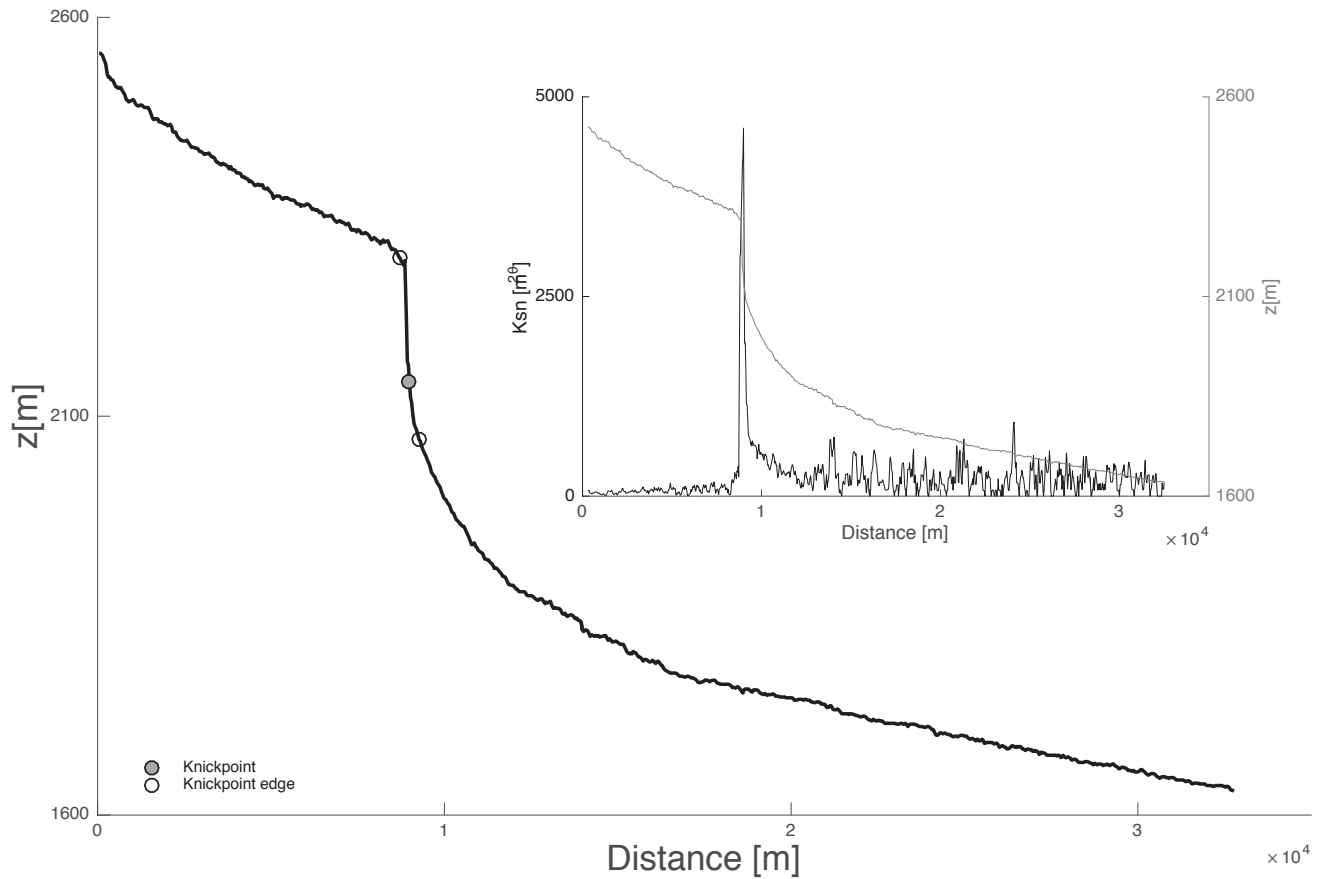


Figure 2: An example for quasi-automatic knickpoint detection. The main figure shows the profile of a channel in basin 1 (Figure 1) and the location of the detected knickpoint (filled circle) and its top and bottom boundaries (open circles). The inset graph shows the same profile (grey line, right y axis), and the associated  $k_{sn}$  values (black line, left y axis).

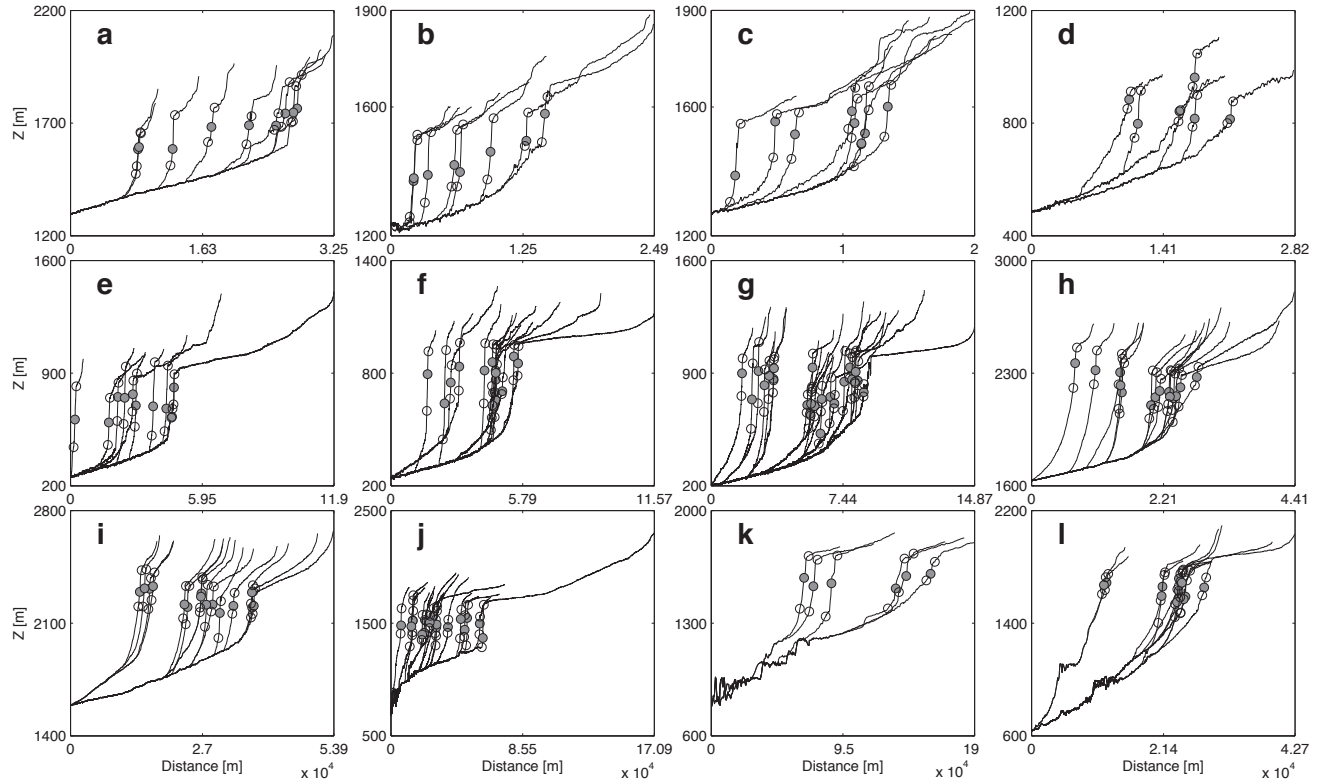


Figure 3: Topographic profiles along the analyzed channel systems. Each panel shows the profiles and the waterfalls for each basin and is labeled in accordance with the basin ID in Table 1. Dark and light colored circles mark the waterfalls and their boundaries, respectively. The lowest extent of the profiles is the prescribed location of the initial knickpoint. The jagged topography of some of the channels reflects the noisy DEM data (this plot shows the raw DEM data rather than a smoothed or pit-filled elevation data).



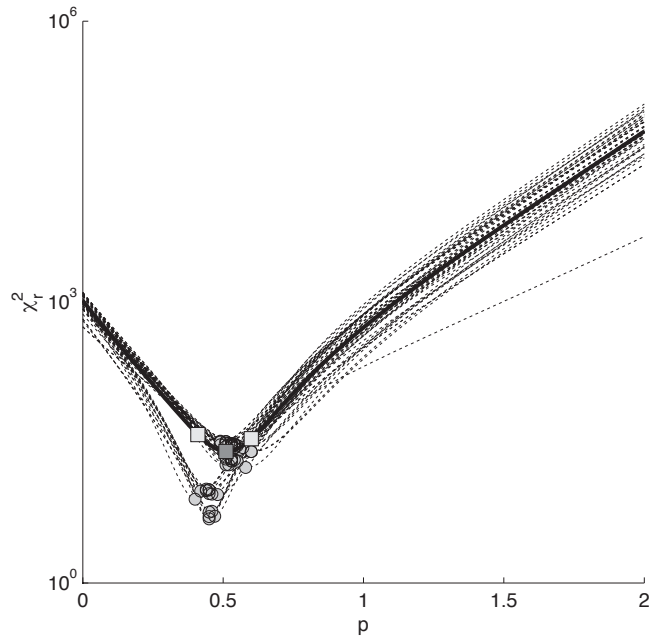


Figure 4: Optimization of  $p$  and its associated uncertainty.  $\chi_r^2$  (y axis) vs. different  $p$  values (x axis) for one of the analyzed basins (basin h, Table 1). The solid line is an optimization curve based on all waterfalls, and the dark grey square marks the optimal  $p$  value that minimizes  $\chi_r^2$  for this case. Dashed lines show 50 optimization curves for arbitrarily chosen subsets of 75% of all waterfalls, and grey circles mark the optimal  $p$  value for each of these iterations. Light squares mark the uncertainty in the optimal  $p$  value for all waterfalls, where this uncertainty is determined from the 2.5 and 97.5 percentiles of the optimal  $p$  values for the 50 subsets of waterfalls (i.e., the grey circles).

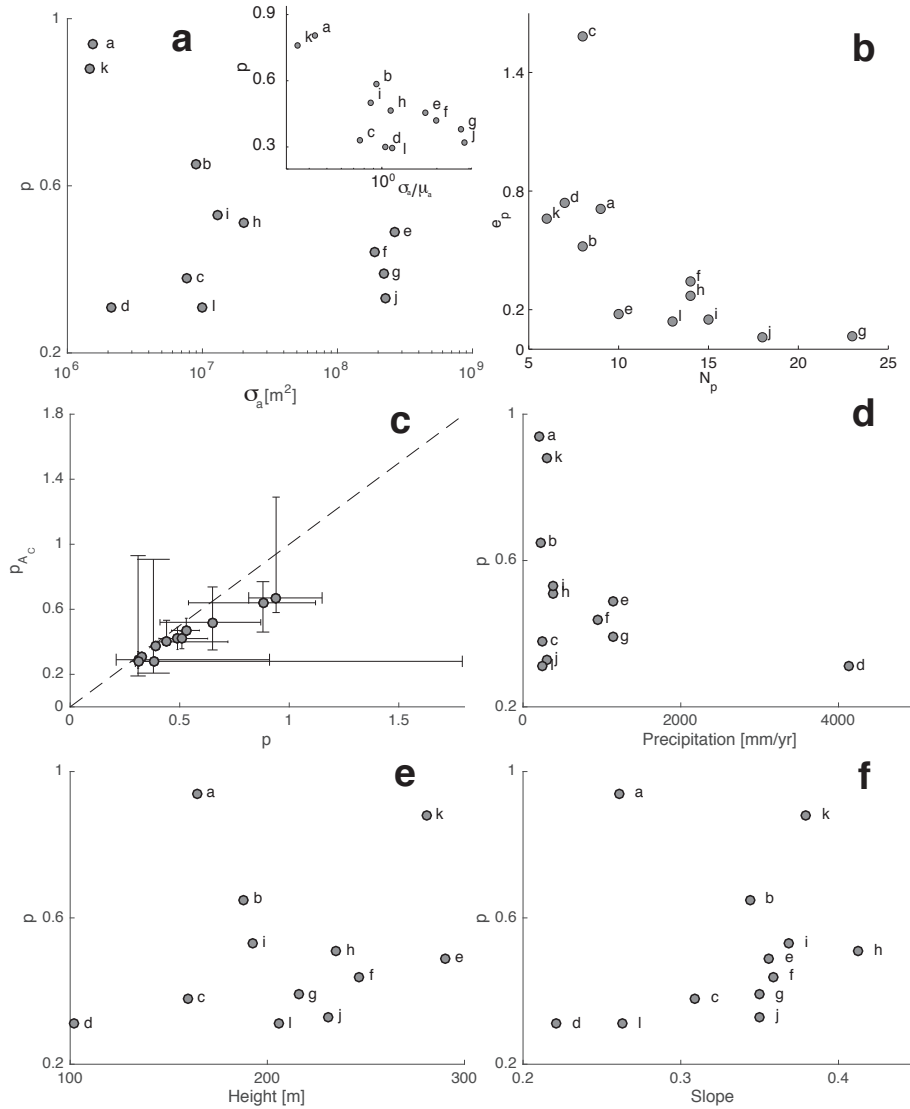


Figure 5: Basin parameters and their influence on  $p$ . (a)  $p$  values (y axis) vs. the standard deviation of drainage area at the waterfalls ( $\sigma_a$ ). The inset shows the relative standard deviation  $\sigma_a/\mu_a$ , where  $\mu$  is the mean drainage area at waterfalls ( $A_w$ ). (b) Uncertainty in  $p$  ( $e_p$ ; the difference between the highest and lowest uncertainty bounds of  $p$  from models with and without a critical area threshold [y axis]) vs. the number of waterfalls within a basin (x axis). (c) Comparison of  $p$  value with  $A_c > 0$  (y-axis) and  $A_c = 0$  (x axis), where  $A_c$  is a critical area threshold for waterfall recession. Dashed line shows a 1:1 relation. (d)  $p$  value (y axis) vs. precipitation. (e)  $p$  value (y axis) vs. mean waterfall height at a basin. (f)  $p$  value (y axis) vs. mean value of slope between the waterfalls top and bottom boundaries at each basin. The  $p$  value in plots d-f are the  $p$  values computed with  $A_c = 0$ .

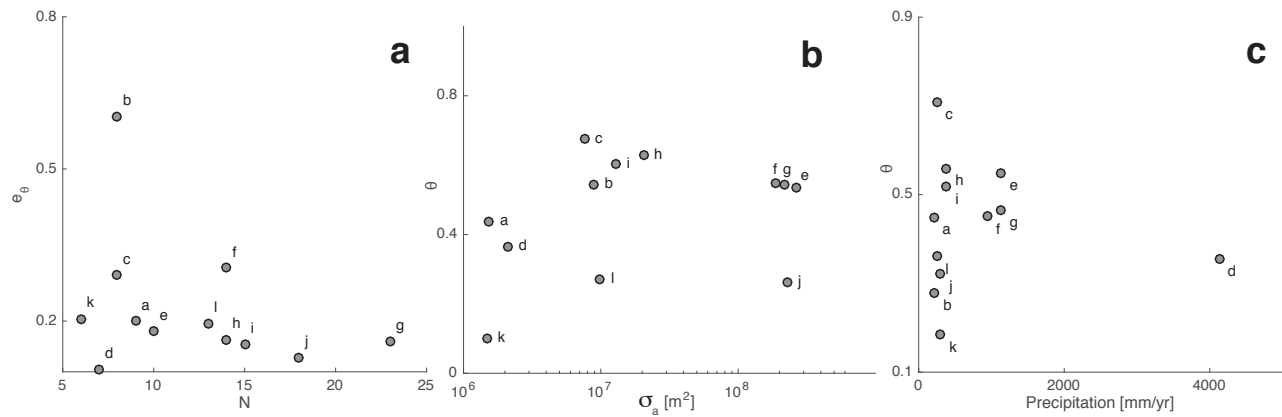


Figure 6: (a) The uncertainty in  $\theta$  ( $e_\theta$ ; the difference between the highest and lowest uncertainty bounds of the three methods used to compute  $\theta$ , y axis) vs. the number of waterfalls. (b)  $\theta$  (y axis) vs. the standard deviation ( $\sigma_a$ ) of drainage area at waterfalls ( $A_w$ ). (c)  $\theta$  (y axis) vs. precipitation.

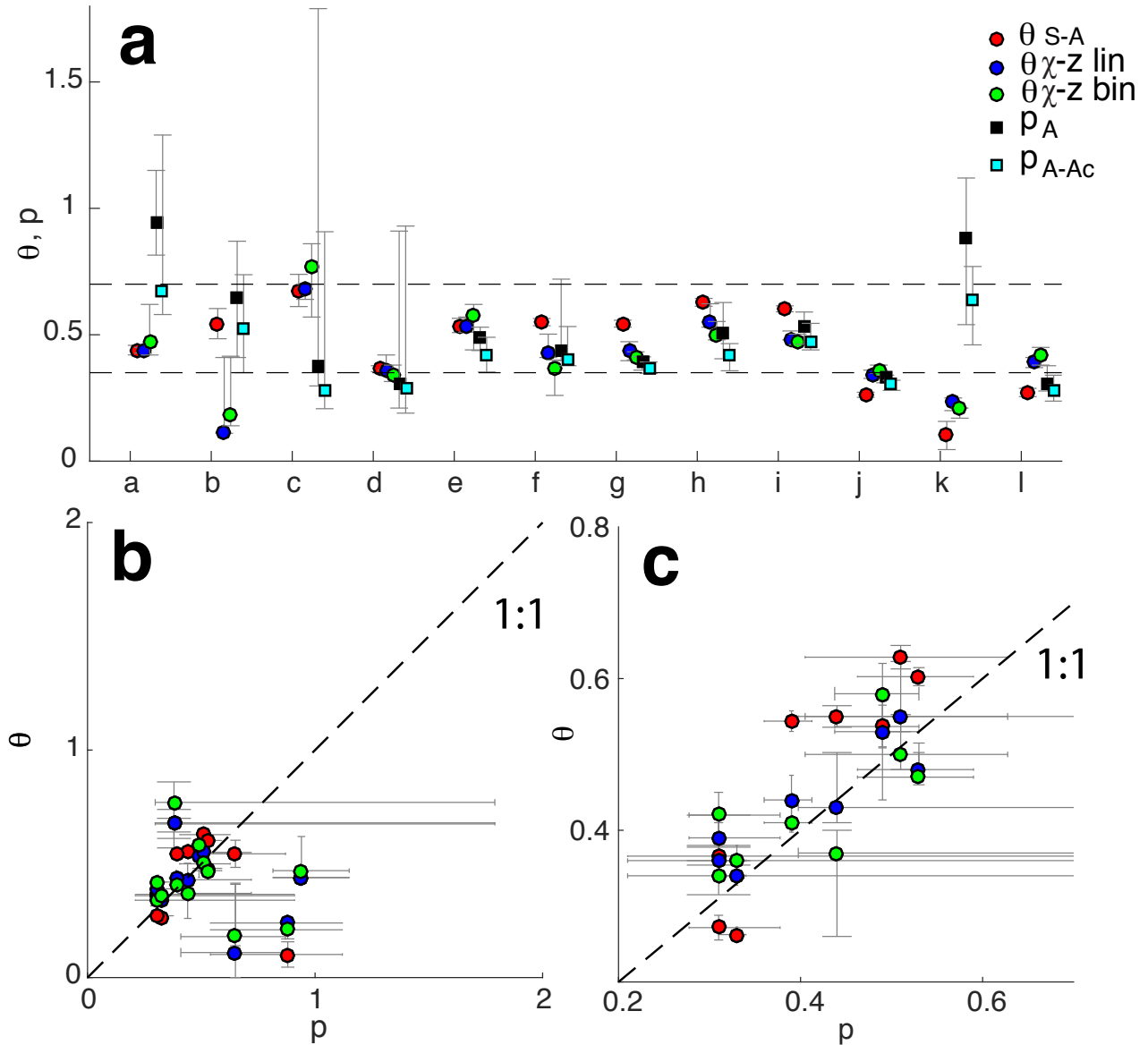


Figure 7: Computed  $p$  and  $\theta$  values. (a) comparison of  $p$  and  $\theta$  for different basins. The x axis shows the ID of the analyzed basins (in accordance with Table 1) and the y axis shows the value of  $p$  and the values of  $\theta$  for the various methods specified in the figure legend (Sections 2.4, 2.3). The uncertainty values are determined via the procedures described in Section 2.5. Note that the uncertainties of  $p$  and  $\theta$  overlap in most cases. The dashed horizontal lines mark the commonly observed  $\theta$  values (0.35-0.7, [Whipple and Tucker, 1999; Tucker and Whipple, 2002]). (b) A scatter plot of  $p$  (x-axis) vs  $\theta$  (y axis) for all basins. The dashed line delineates a 1:1 relations between  $p$  and  $\theta$ .  $\theta$  values computed with different methods are colored as in panel a. Note that in many cases the uncertainties of  $p$  and  $\theta$  overlap with this 1:1 line. (c) Same as panel b, for basins with  $\geq 10$  waterfalls. This gives  $R^2 = 0.64$  and a probability (p) value of  $2.4 \times 10^{-6}$ .

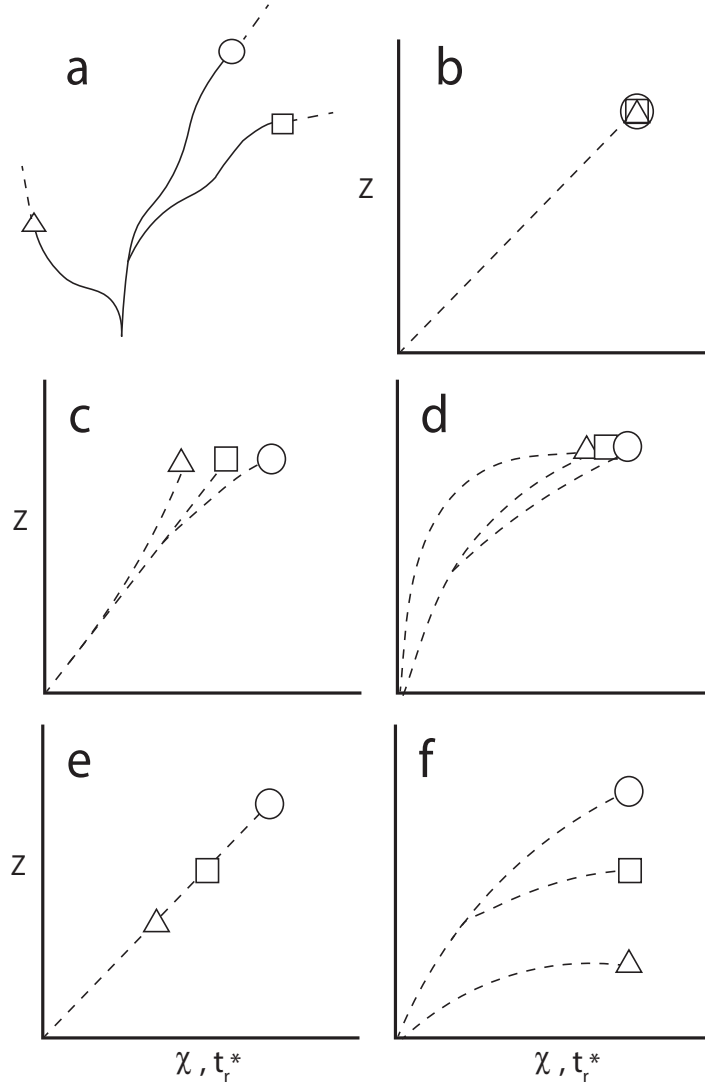


Figure 8: Schematic relations between  $p$  and  $\theta$  in  $\chi - z$  space. (a) Schematic map of a basin with 3 waterfalls. waterfalls are marked with shapes, and the solid and dashed lines mark the channel downstream and upstream of the waterfall, respectively. (b)  $\chi - z$  relations when all waterfalls lie at the same elevation. Here and in the following panels waterfalls are marked by shapes that correspond to those in panel a, and dashed line marks the  $\chi - z$  values along the pathway from the origin to the waterfalls. (c)  $\chi - z$  relations when waterfalls are at the same elevations and the  $\theta$  value used to compute  $\chi$  is that which minimizes the scatter in  $z$  for a least square regression between  $\chi$  and  $z$ . (d)  $\chi - z$  relations when waterfalls are at the same elevations and the  $p$  (or  $\theta$ ) value used to compute the non-dimensional recession duration  $t_r^*$  (or  $\chi$ ) is that which minimizes the scatter in  $t_r^*$  (or  $\chi$ ) for the waterfall locations only. (e)  $\chi - z$  relations when waterfalls are at different elevations and the  $\theta$  value used to compute  $\chi$  is that which minimizes the scatter in  $z$  around a linear regression between  $\chi$  and  $z$ . (f)  $\chi - z$  relations when waterfalls are at different elevations and the  $p$  (or  $\theta$ ) value used to compute the non-dimensional recession duration ( $t_r^*$ ) is that which minimizes the scatter in  $t_r^*$  (or  $\chi$ ) for the waterfall locations only.

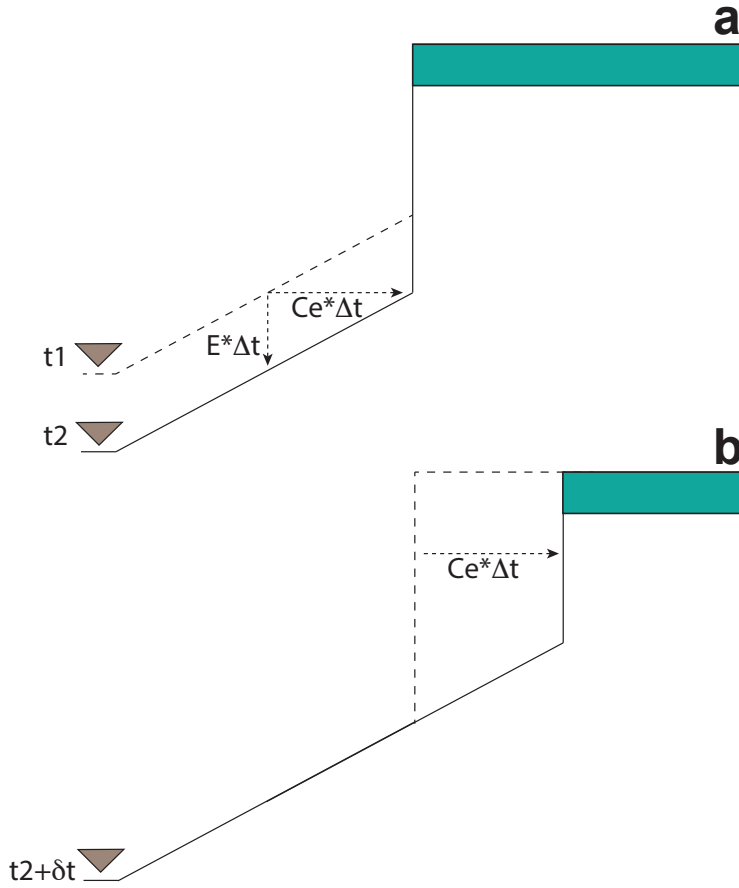


Figure 9: Schematic illustration of a recession mechanism that can cause similarity between the recession of non-vertical channels ( $C_e$ ) and waterfall recession ( $C_{ew}$ ) (i.e.,  $C_e \simeq C_{ew}$ ) over long time scales (after *Haviv et al. [2010]*). (a) Channel profile at times  $t_1$  (dashed line) and  $t_2$  (solid line). Grey triangles represents the base-level elevation in  $t_1$  and  $t_2$ .  $\Delta t$  is the time span between  $t_1$  and  $t_2$ , such that  $E * \Delta t$  is the depth of erosion ( $E$ ) downstream of the waterfall over this period and  $C_e * \Delta t$  is the recession caused by this erosion. In this setting the cap-rock layer (colored in grey) is resistant to erosion whereas the underlying layers are of higher erodibility. (b) Channel profile following a gravitational collapse of the waterfall and downstream transport of the resulting debris (during a relatively short time period  $\delta t$ ). The waterfall at time  $t_2$  (dashed line) can collapse through various processes (e.g., undercutting, toppling). Note that in that case the long term waterfall height is likely set by lithologic properties in conjunction with the gravitational collapse mechanism, and is constant in time and space as long as these properties are constant. Also note that the slope of the channel section downstream of the waterfall is  $S = E/C_e$  (see dotted arrows in panel a), such that  $C_e = E/S$  and  $C_e = KA^m S^n / S = KA^m S^{n-1}$  in the context of the channel incision model.

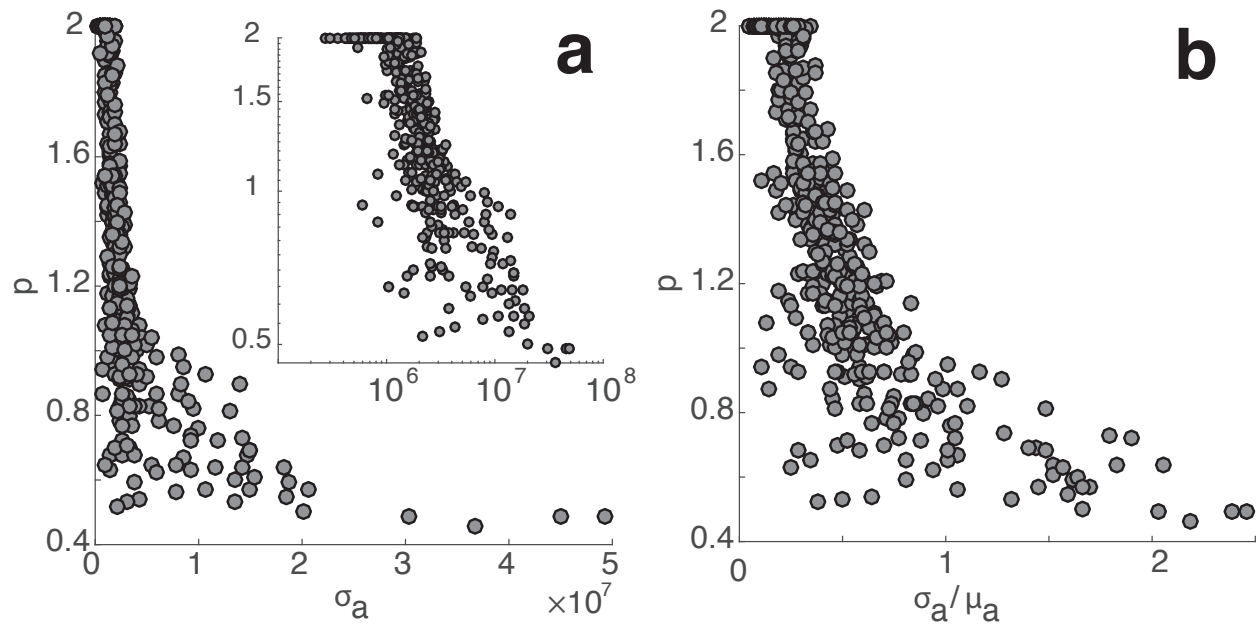


Figure 10: Relations between  $p$  and  $\sigma_a$  for experiments with arbitrary waterfall positioned in basin g plotted in linear (a) and logarithmic (inset of panel a) scales. Each filled circle shows the values of  $p$  and  $\sigma_a$  for a single experiment with 11 waterfalls that are arbitrary positioned. (b)  $p$  vs. the relative standard deviation in  $A_w$  ( $\sigma_a/\mu_a$ ).

Table 1: Properties of the analyzed basins

Basin ID	Basin name	Location	LAT	LON	MAP [mm/yr]	Lithology	Studies of p in this basin
a	Happy Canyon	Utah, USA	38.137	-110.369	200	Triassic sedimentary rocks [Chinle, Wingate, Kayenta formations], primarily mudstone, sandstone, limestone <sup>1</sup> .	-
b	Mineral Canyon	Utah, USA	38.531	-109.976	200	Triassic sedimentary rocks [Chinle, Wingate, Kayenta formations], primarily mudstone, sandstone, limestone <sup>1</sup> .	-
c	Taylor Canyon	Utah, USA	38.475	-109.941	250	Triassic sedimentary rocks [Chinle, Wingate, Kayenta formations], primarily mudstone, sandstone, limestone <sup>1</sup> .	-
d	Rio Napo	Pastaza, Ecuador	-1.236	-77.709	4150	Tertiary sedimentary rocks [Arajuno formations], primarily conglomerate and sandstone <sup>2</sup> .	-
e	Chandler River	New South Wales, Australia	-30.708	152.043	1150	Paleozoic metasedimentary rocks [Myra Beds and undivided units], primarily schist, slate, phyllite, greywacke, mudstone <sup>3</sup> .	Weissel and Seidl [1998], Weissel and Seidl [1997], Seidel and Weisel [1996]
f	Macleay River	New South Wales, Australia	-30.783	151.953	950	Paleozoic metasedimentary rocks [Myra Beds and undivided units], primarily schist, slate, phyllite, greywacke, mudstone <sup>3</sup> .	Weissel and Seidl [1998], Weissel and Seidl [1997], Seidel and Weisel [1996]
g	Apsley River	New South Wales, Australia	-30.884	152.028	1150	Paleozoic metasedimentary rocks [Myra Beds and undivided units], primarily schist, slate, phyllite, greywacke, mudstone <sup>3</sup> .	Weissel and Seidl [1998], Weissel and Seidl [1997], Seidel and Weisel [1996]
h	Parachute Creek	Colorado, USA	39.467	-108.076	400	Tertiary sedimentary rocks [Wasatch and Green River formations], primarily shale, sandstone, marlstone <sup>4</sup> .	Berlin and Anderson [2007]
i	Roan Creek	Colorado, USA	39.406	-108.269	400	Tertiary sedimentary rocks [Wasatch and Green River formations], primarily shale, sandstone, marlstone <sup>4</sup> .	Berlin and Anderson [2007]
j	Havasu Creek	Arizona, USA	36.272	-112.719	300	Permian sedimentary rocks [Kaibab, Toroweap, Coconino, Hermit fm], primarily limestone, shale, sandstone <sup>5</sup> .	-
k	Tuckup Canyon	Arizona, USA	36.298	-112.876	300	Permian sedimentary rocks [Kaibab, Toroweap, Coconino, Hermit formations], primarily limestone, shale, sandstone <sup>5</sup> .	-
l	Surprise Canyon	Arizona, USA	35.925	-113.610	250	Permian sedimentary rocks [Kaibab, Toroweap, Coconino, Hermit formations], primarily limestone, shale, sandstone <sup>5</sup> .	-

Basin ID are identical to those in Figure 1, latitude and longitude (decimal degrees) show the trunk channel location, MAP is the mean annual precipitation (rounded to the nearest 50mm/yr multiplier) computed from 0.5 degree dataset from precipitation data collected between 1901-1914 and attained from <https://crudata.uea.ac.uk/cru/data/hrg/>. The lithologic data is sourced from:

<sup>1</sup> Source: <http://files.geology.utah.gov/online/usgs/>

<sup>2</sup> Source: Ruiz [2002]

<sup>3</sup> Source: <http://www.resourcesandenergy.nsw.gov.au>

<sup>4</sup> Source: Berlin and Anderson [2007]; Hail Jr [1992]

<sup>5</sup> Source: <http://pubs.usgs.gov/imap/>